UNIVERSITÀ
DEGLI STUDI
FIRENZE

Università degli Studi di Firenze
Dipartimento di Ingegneria dell'Informazione (DINFO)
Corso di Dottorato in Ingegneria dell'Informazione

Curriculum: Automatica, Ottimizzazione e Sistemi Complessi
Settore Scientifico Disciplinare: ING-INF/04

Single cell elastography from nanoindentation experiments

Candidate
Alice Bartolozzi

Supervisors
Prof. Michele Basso

Dr. Massimo Vassalli

PhD Coordinator
Prof. Luigi Chisci

---

ciclo XXXI, 2015-2018

Università degli Studi di Firenze, Dipartimento di Ingegneria
dell'Informazione (DINFO).

"Oggi, quando ormai quel poco che potevo fare l'ho fatto, e mi avvio alla conclusione generale, ho un passato da raccontare: e questo, sia ben chiaro, come lo è a me stesso, è il passato di un fisico "normale", che molti potranno giudicare mediocre, o comunque non geniale. Come me ce ne sono tanti; eppure qualche diritto a fare storia lo abbiamo, nel senso che, specie vivendo in un mondo che adora i geni come usava con i semidei, i 'comuni mortali'hanno talvolta coscienza dei loro limiti e, perciò, bisogno di consolazione. La Fisica progredisce con i bagliori delle grandi idee, ma anche con la moltitudine delle fiammelle di ideuzze, che non danno fama ma rischiarano il panorama."

Carlo Bernardini

Acknowledgments

Innanzitutto vorrei ringraziare Massimo Vassalli e il prof. Michele Basso per avermi dato la possibilitá di svolgere il dottorato nel pieno delle sue potenzialitá, in un contesto cosí umanamente positivo quale é l'Istituto di Biofisica del CNR di Genova. Ringrazio tutti i miei colleghi dell'IBF, che hanno fatto sí che l'ambiente di lavoro fosse alla stregua di una seconda casa. Ringrazio, tra i miei colleghi, quelli che ad oggi non posso chiamare in altro modo che cari amici: Morgan, Sara, Francesca, Julian ed Enrico. Ringrazio la mia famiglia, che é il mio porto sicuro, la mia forza, la mia isola felice, il luogo in cui tornare e sentire di non esser mai partiti. Ringrazio l'amore della mia vita, Francesco, perché la vita non sarebbe stata altrettanto facile e bella in questi anni, vissuti con la consapevolezza di non essere mai sola davanti alla minima difficoltá.

Abstract

Cell mechanics is currently an exciting and active area of research, and it has great potential to provide a new and different outlook on pathologies and classical biological problems. It is known cells can actively sense and respond to a huge variety of mechanical signals. New different scientific branches are addressing the mechanisms underlying these processes of sensing and responding, called respectively mechanosensing and mechanotransduction. Mechanobiology is a novel field that stands at a meeting point among biology, bioengineering and physiscs and its purpose is to address these processes with a quantitative, model based approach. The increasing growth of mechanobiology has been supported by the advancement of new technologies, especially in measuring force. Indeed the exploitation of nanotechnology to the study of biological systems opened new avenues towards innovative approaches based on single cell mechanical characterization. Nanoindentation experiments played a major role in this process, and still do. This thesis aimed to find a simple and robust analytical procedure which can provide new insight in cell mechanical properties, starting from nanoindentation experiments, allowing to make inferences into the functional state of the cell. At the beginning the whole existing procedure was optimized to achieve a higher throughput. Then, an existing model, the most used in literature to describe cell mechanical properties, was extended, in order to increase and supplement the information gained from nanoindentation experiments. This new procedure, called Elastography, allowed to identify different stiffness layers into the single cell, putatively associated with inner components and compartments of the cell. The Elastography was tested and proved to work both simulating the system and in experimental tests. Then it was applied in many different biological problems, to several coltures of different cell lines, in order to address specific questions about changes in cell mechanical properties.

Contents

Contents **vii**

List of Figures **ix**

1 Introduction **1**
1.1 Cell mechanics 2
1.2 Mechanobiology 4
1.3 Objective 6
1.4 Thesis structure 7

2 Experimental setup **9**
2.1 Introduction to nanoindentation experiments 10
2.2 The Chiaro nanoindenter 11
2.2.1 Calibrating the system 15
2.3 Probe Selection 17
2.4 Force Displacement Curve 18

3 Modeling cell mechanics **23**
3.1 Introduction 23
3.2 Hertz Model 24
3.3 Force Integration to Equal Limits (FIEL) 28
3.4 Elastography 30
3.5 Comments 35

4 Procedure optimization **37**
4.1 Introduction 37
4.2 Preprocessing 38
4.2.1 Pre-processing steps 39

4.3 From force displacement curves to force indentation curves . 39
4.3.1 Force-indentation curve computation 39
4.4 DFIT vs FIEL 39
4.5 Experimental conditions 40
4.6 Extracellular solution 41
4.7 Confluency 43
4.8 Experiment duration 44
4.9 Conclusion 45

5 Simulations **47**
5.1 Elastography: from the experimental curves to the bilayer model 47
5.2 Elastography: Absolute and Relative 49
5.3 Simulation 51
5.4 Stiffer external layer 51
5.5 Stiffer internal layer 55
5.6 Varying the thickness of the external layer 59
5.7 Single layer 63
5.8 Varying the indentation step 64
5.9 Adding noise 67
5.10 Conclusion 70

6 Biological problems **71**
6.1 Introduction 71
6.2 Human Fetal Osteoblast 71
6.3 FaO cells 77
6.4 HEK cells 83
6.5 A1 cells 90
6.6 Piezo1 94

7 Discussion **97**

8 Conclusion **101**
8.1 Summary of contribution 101
8.2 Directions for future work 102

A Publications **103**

Bibliography **105**

List of Figures

1.1 3D sensory homunculus 1
1.2 Cell mechanical stimuli illustration 3
1.3 Matrix elasticity directs stem cell lineage specification 4
1.4 Cell traction forces 5
1.5 Eukaryiotic cytoskeleton 6

2.1 Osteoblast indentation with Piuma Chiaro 10
2.2 Chiaro indenter main elements 11
2.3 Setup connection path 12
2.4 Main compoment of the Chiaro head 13
2.5 Illustration of the probe indenting a cell. 14
2.6 Optical calibration performed from the interferometer. 15
2.7 Geometrical calibration 16
2.8 Probe selection guide graph 17
2.9 Indentation profile settled for a force distance curve. 18
2.10 Main steps of a force-displacement curve 19
2.11 Example of a force-displacement curve collected in a classical indentation 20

3.1 Illustration of the contact mechanics of two elastic bodies . . 24
3.2 Force indentation curve (blue line) fitted with the Hertz model (red line). 27
3.3 Force indentation curve with the Fiel algorithm 30
3.4 Force indentation curve segmented for Elastography, first approach 31
3.5 Force indentation curve segmented for Elastography, second approach 33

4.1 Example of an ideal curve: it starts with a flat region so that the contact point can be identified. 38
4.2 Relative elasticity varies depending on the medium: dmem and physiological solution are compared. 42
4.3 Relative elasticity varies depending on cell number 43
4.4 Relative elasticity doesn't vary depending on the experiment duration 44

5.1 Examples of experimental stiffness curves depending on the indentation depth. 48
5.2 49
5.3 When a bilayer exists, the DFIT method identifies just the internal layer stiffness. 52
5.4 When a bilayer exists, the FIEL method identifies just the internal layer stiffness. 52
5.5 Elastography vs Relative elastography curves 53
5.6 External and internal layer stiffness for the 3 sets of parameters. 53
5.7 Thickness of the external layer for the 3 sets of parameters. . 54
5.8 When a bilayer exists, the DFIT method identifies just the internal layer stiffness. 55
5.9 When a bilayer exists, the FIEL method identifies just the internal layer stiffness. 56
5.10 Elastography vs Relative elastography curves 57
5.11 Elastography vs Relative elastography: E_0 and E_b. 57
5.12 Elastography vs Relative elastography: d_{0b} 58
5.13 Elastography vs Relative elastography varying the thickness d_{0b} 59
5.14 Elastography vs Relative elastography varying the thickness d_{0b}. 60
5.15 Elastography vs Relative elastography varying the thickness d_{0b}: E_b and E_0. 60
5.16 Elastography vs Relative elastography varying the thickness d_{0b} 61
5.17 Elastography vs Relative elastography varying the thickness d_{0b}. 62
5.18 Elastography vs Relative elastography varying the thickness d_{0b}: E_b and E_0. 62
5.19 Elastography vs Relative elastography for the single layer. . . 63
5.20 Elastography curve varying the indentation step. 64
5.21 Elastography curve varying the indentation step. 65

5.22 Elastography curve varying the indentation step. 66
5.23 Elastography curve varying the indentation step. 66
5.24 Elastography curve with noise: $E_0 > E_b$. 67
5.25 Elastography curve with noise: $E_0 > E_b$ 68
5.26 Elastography curve with noise: $E_0 < E_b$. 68
5.27 Elastography curve with noise: $E_0 < E_b$. 69

6.1 Image of the hFOB cells at day 0 72
6.2 Image of the hFOB cells atfer 15 days of maturation 72
6.3 hFOB elasticity during maturation 73
6.4 Significativity map 74
6.5 Osteogenic markers expression for the hFOB 75
6.6 Matrix correlation of morphological parameters and elasticity. 76
6.7 For FaO cells incubated in the absence (Ctrl) or in the presence of fructose (Fru), oleate/palmitate (FA), Fru/FA, FA/TNFα are shown: (A-B) average number of LDs/cell and size of LDs; (C) TG content expressed as percent TG content relative to controls, normalized for proteins determined with Bradford assay. 78
6.8 Neutral lipids were visualized by optical microscopy using the selective Oil-RedO (ORO) dye. 79
6.9 Mean and standard deviation of the gaussian probability density function, fitted on the relative Young's modulus distribution with the DFIT and the FIEL methods 80
6.10 Probability density functions of both FIEL and DFIT methods. 81
6.11 Relative Elasticity (E_r) of single cell respect to the control, obtained through the FIEL method 82
6.12 Three major protein filaments compose the cell cytoskeleton . 83
6.13 Cell schematization 84
6.14 HEK cells images for all the conditions 85
6.15 Elasticity (E) of single cell respect to the control, obtained through the Hertz method. 86
6.16 Relative Elasticity (E_r) of single cell respect to the control, obtained through the FIEL method. 87
6.17 Elasticity (E_b) of the internal layer obtained through the Elastography method. 87
6.18 Elasticity (E_0) of the external layer obtained through the Elastography method. 88

6.19 Thickness (d_{0b}) of the external layer obtained through the Elastography method. 88
6.20 Cells stained with fluorescent labels to help visualise the cytoskeleton with microtubules (green), actin filaments (red), and the nucleus (blue). *British Society for Cell Biology* . . . 89
6.21 Images of the wild type a1 cells during the treatment with aβ. 90
6.22 Images of the silenced for the prion a1 cells during the treatment with aβ. 91
6.23 External layer stiffness. 92
6.24 Internal layer stiffness. 93
6.25 External layer thickness. 93
6.26 Picture of the three cell lines: the control cells (CTRL), the overexpressing piezo1 cells (PIEZO1) and the piezo1 knockout cells (KO). 94
6.27 Internal layer stiffness. 95
6.28 External layer stiffness. 95
6.29 External layer thickness. 96

Chapter 1

Introduction

Humans are sensory beings. The human body is equipped with a large multitude of sensors in every part. This sensors network allows them to perceive the sourrounding environment and make decisions in this regard: 'Does it taste good?', 'Is it soft?', 'I prefer classic music'. Perception passes through the nervous system, in particular through the stimulation of the sensory system, which is responsible of the final transduction. The sensory homunculus shown below, Fig. 1.1, is a representation of how much of the cerebral cortex relates to each part of the body. Practically the homunculus body is distorted to recreate the right proportions between the brain areas dedicated to the processing of different sensory functions. The bigger is the cerebral area, the bigger is the corresponding part of the body.

Figure 1.1: 3D sensory homunculus model, Sharon Price-James (Natural History Museum, London)

Sensing happens in many different ways in the human body and through different kind of stimulus. The same happens scaling down at cellular level. For example hair cells are sensory receptors of both the auditory and vestibular systems that can sense movement through mechanotransduction. In the skin, four types of mechanoreceptors respond depending on the period of the stimuli, enabling us to distinguish between rough and soft, between a light and gross touch, but also to distinguish moderate vibrations and sustained skin stretch. Furthermore, juxtaglomerular cells are mioepithelial cells in the kidney working as baroreceptors, or mechanoreceptors able to sense variations in blood pressure. It is evident that sensitiveness to mechanical stimuli plays a major role in many phisiopathological processes. This peculiar sensitiveness is called mechanosensation and it is defined as the transduction of mechanical force into intracellular signals. A deeper knowledge of cell mechanosensation can be achieved passing through cell mechanics investigation.

1.1 Cell mechanics

Cell mechanics is the research area that deals with understanding the world of sensing and generating mechanical forces at cellular level. Its significance stems from the fact that it has proved a great potential in providing a new and different outlook on pathologies and classical biological issues [46]. Actually cell mechanics is involved in many biological processes, examples of which are cell crawling and wound healing [20], protein regulation [31], and adhesion [65]. But also numerous pathologies (cancer, asthma, and sickle cell anemia, malaria, ecc.) involve alteration of cellular mechanical properties [36]. Indeed cells actively sense and respond to a huge variety of mechanical signals, Fig. 1.2 [40].

These two main cellular duties, sensing and responding, are subject of two main strands of cell mechanics: mechanosentivity and mechanotransduction. Both are cellular processes that involve intra and extracellular components. Mechanosensing concerns the ability of living cells to sense the mechanical signals provided by their environment. Mechanotransduction instead, involves mechanosensing and also the process of translating mechanical signals into a cellular response. The study of those mechanisms is of major importance becuse of their involvment in many fundamental processes. For example, cells sense and process mechanical information provided

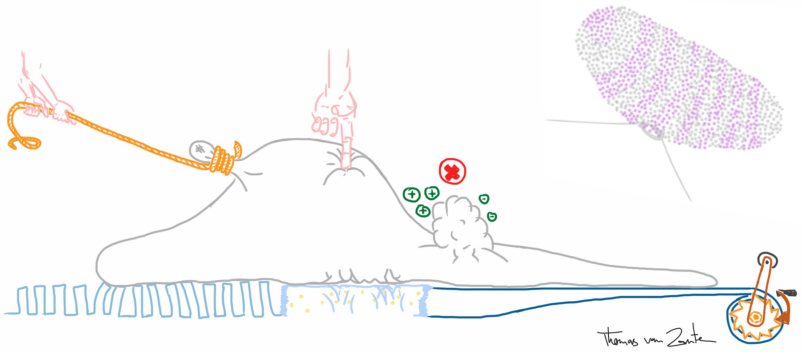

Figure 1.2: Illustration of the mechanical stimuli to which a cell is subjected, [1].

by the extracellular environment to make decisions about growth, motility and differentiation. The mechanical stiffness of the surrounding extracellular matrix determines normal cell functions, stem cell differentiation and tissue homeostasis, whereas the deregulation of the mechanical properties of the extracellular matrix contributes to the onset and progression of various diseases (such as cancer and fibrosis), [19].

Besides the cell sensitivity to forces and substrate stiffness has been recognized as a powerful tool in tissue engineering, for organ-on-chip and regenerative medicine applications. For example it is exploited to design biomaterials that optimally guide stem cells or resident cells in the patient, in order to get a functional replacement tissue. Therefore cells probe the rigidity of their extracellular environment and this seems to happen applying traction forces thorugh transmembrane proteins (integrins). However it is still poorly understood how this makes cells to sense matrix stiffness and how this mechanical information is transduced into a cellular response. Answering these questions is far from being easy because of the large number of mechanosensors and transducers identified so far (e.g. vinculin, talin, integrins, the actin cytoskeleton and mechanosensitive ion channels). It also remains unclear how all these components work together to regulate mechanosensing. What is known is that this complex network of mechanotransduction trasmits the physical signal from environments to the nucleus, modifing the whole cell at many different levels: ions concentrations in the cytoplasm, gene expression, cell morphology and fate [30], [42], [61]. An emerging field of science that is

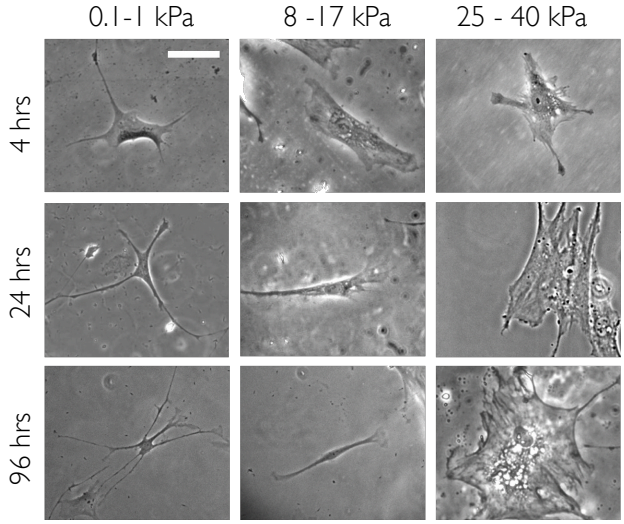

Figure 1.3: Matrix elasticity directs stem cell lineage specification: soft matrices that mimic brain are neurogenic, stiffer matrices that mimic muscle are myogenic, and comparatively rigid matrices that mimic collagenous bone prove osteogenic. *Engler et al., Cell (2006) 126:677-89*

handling these issues is mechanobiology.

1.2 Mechanobiology

Mechanobiology is an emerging multidisciplinary field that lays at the interface of various scientific disciplines: cell and developmental biology, bioengineering and biophysics [32], [51]. The origins of this field can be found in the interest to cell migration and development, two mechanisms that involve cell shape modification and forces. Despite this, mechanobiology appeared only 20 years ago, because of the need to explain an unexpected result. Focal adhesions (that are integrin based cell matrix adhesions) result to be mechanosensitive, and surprisingly they are proved to grow if the environment is stiff and mechanical force are applied, rather than dissociate as expected [17], [59], Fig. 1.4. Starting from that, a large amount

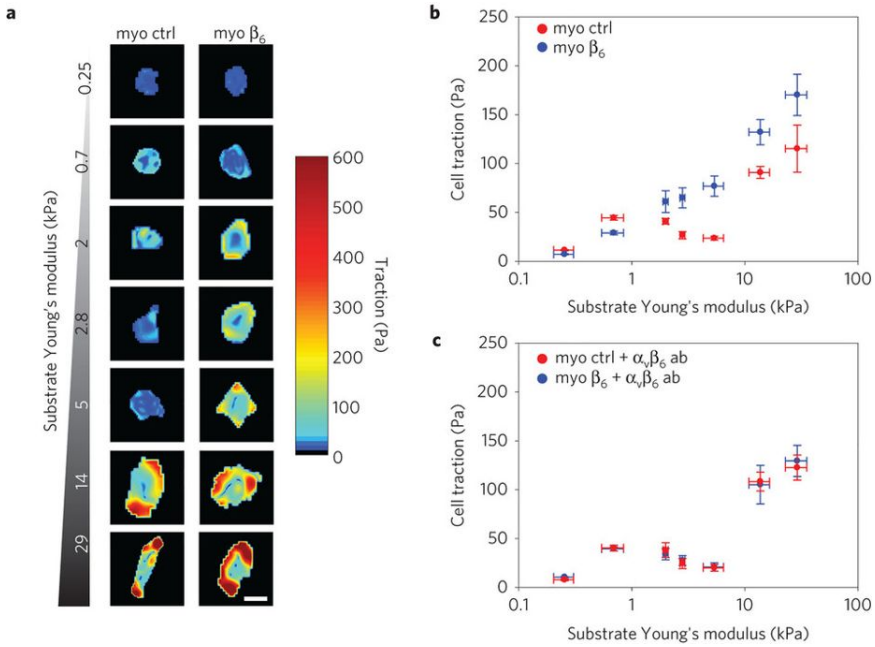

Figure 1.4: Colour maps showing the traction forces applied by individual myo ctrl or myo β6 cells on FN-coated polyacrylamide gels of increasing rigidity. Scale bar, 20μm. *Elosegui-Artola et al., Nature Materials (2014) 126:677-89*

of mathematical models has been developed and the application of physics and modelling has become an integral part of many studies in this field. These quantitative approaches assist the experimental part on many levels. Above all, they can give rise to a novel understanding of biological processes, interpretate counterintuitive results and help planning future experiments. This integration with physics has been fondamental for mechanobiology to go beyond the field of cell adhesion and to extend also to other mechanosensitive elements: the cytoskeleton, the genome and the extracellular matrix. Mechanobiology suggests that changes in cell mechanics, in particular in the extracellular matrix structure and in the mechanotransduction paths, may result in the development of many diseases. Progress in mechanobiology is going very fast, supported by the advancement of new technologies, especially in measuring forces.

1.3 Objective

In the previous sections the reason of investigating cell mechanical properties were fully explained. The focus now is on one of the mechanosensitive element mentioned before: the cytoskeleton.

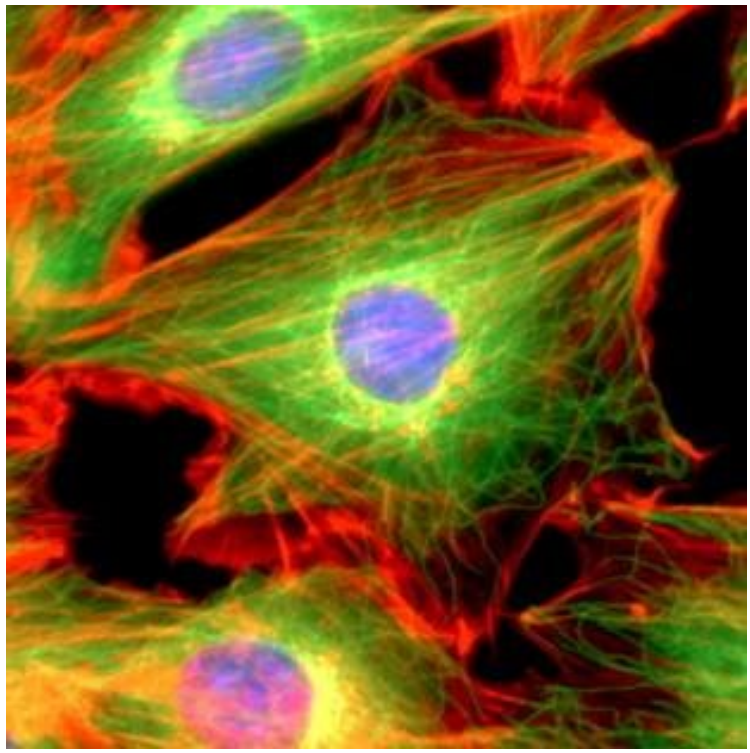

Figure 1.5: The eukaryotic cytoskeleton including actin microfilaments shown in red and microtubulin shown in green, [7]

.

It will be explored later in details what the cytoskeleton is. So far it is sufficient to know that cells can detect mechanical stimulation activating mechanosensitive signal pathways and can respond through cytoskeletal reorganization and force generation. Disrupting the cytoskeletal architecture can lead to changes in cell mechanical properties such as: elasticity, adhesiveness and viscosity. Indeed these transformations are often a hallmark

and symptom of a variety of pathologies [21]. A multitude of experimental techniques and theoretical models have been developed to characterize cell mechanical properties. On this line, the exploitation of nanotechnology to the study of biological systems opened new avenues towards innovative approaches based on single cell mechanical characterization [58], [36]. In fact single cell analysis aims to highlight cell-to-cell variations within a cell population, e. g. organs a tissues, essential to the study of diseases and drug development [5], [29]. Nanoindentation experiments played a major role on the process of single cell mechanical characterization, and still do. Therefore this thesis focused on nanoindentation experiments, aiming to characterize mechanosensitive elements and changes in their biomechanics. Indeed the objective was to find a robust approach to identify single cell mechanical properties, that would be able to correlate cell mechanics with the functional state of the cell.

1.4 Thesis structure

Given this general introduction, the thesis is structured following this line:

- in the second chapter, nanoindentation experiments are explained, together with the experimental setup that has been used to pursue this project;
- in the third chapter, modeling cell mechanics is faced and three approaches are presented;
- in the fourth, the experimental path is optimized in order to get more reliable and robust results;
- in the fifth chapter, all the theory is simulated in order to test and compare the approaches;
- in the sixth chapter the biological problems faced are presented and the results showed;
- in the seventh chapter, the whole result is discussed.

Chapter 2

Experimental setup

In the last two decades indentation testing has become very famous for mechanical properties measurements because of the remarkable resolution achieved, enough to speak about nanoindentation. The Atomic Force Microscope (AFM) has been a pioneer in nanoindentation, yielding to novel insights in understanding development and progression of several diseases, [37], [10]. It is currently a powerful tool for cell mechanics characterization. In this chapter nanoindentation as a tool to explore cell mechanics will be presented and explained, along with what means performing a nanoindentation measurements both in terms of the experimental procedure and the experimental setup. The system that has been used to perform nanoindentation measurements in this reasearch project is introduced and its working principle, its application and the collected measurements are explained in details in the following.

2.1 Introduction to nanoindentation experiments

Performing a nanoindentation measurement consists in approaching the sample that has to be characterized and "touch" it gently, till it distorts. Sample mechanical properties are related to the force, as a function of the indentation depth, that can be measured during the sample deformation.

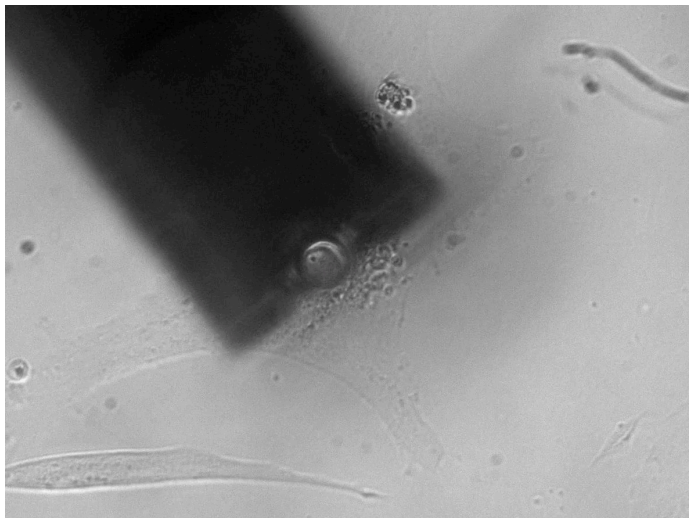

Figure 2.1: Osteoblast indentation with Piuma Chiaro

In the following chapter the curves resulting from a nanoindentation experiment will be explained and methods to analyse them will be described and proposed. In this chapter instead, the focus will be on the experimental setup that allows to collect this kind of measurements.

A standard nanoidentation setup is composed of:

- a sensor,
- an actuator.

Sensors and actuators are used to apply and measure the mechanical load, that is the result of the interaction between the sample and the probe. Practically the probe is composed of a tip attached to a cantilever. When the tip is in contact with the sample, the sample starts deforming and consequently

the cantilever starts bending. Measuring the deflection of the cantilever and knowing its elastic constant, it is possible to derive the force. This is the general functioning of a nanoindentater, that can be realised exploiting different technologies. The most famous instrument for nanoindentation experiments is the Atomic Force Microscope (AFM). Usually the AFM uses a laser beam deflection system where the laser is reflected from the back of the cantilever and onto a position-sensitive detector, for example a photodiode. The laboratory of the Biophysical Institute of the National Research Council (CNR) is provided with a particular nanoindenter: the Chiaro nanoindenter, produced by the company Optics11, [2].

2.2 The Chiaro nanoindenter

Figure 2.2: Chiaro indenter main elements: (1) the controller, (2) the interferometer, (3) the head, (4) the pc.

Chiaro is pretty much similar to an atomic force microscope, what actually changes it is the technology exploited. Indeed, the Chiaro nanoindenter is designed to apply and sense forces on small objects and materials as an AFM. It is an auto-aligned and pre calibrated instrument that allows to measure cell mechanical properties in a non-destructive way. Chiaro allows an easy access to the biological sample, without requiring a custom chamber for the sample positionig. Furthermore steps necessary to set up the measurement are quick and simple. At the *Biophysical Institute* (IBF) laboratory the Chiaro is placed on a white field inverted microscope. The main elements of this device are:

- the head;
- the interferometer;
- the controller;
- a PC, where the Optics11 software is installed.

In the scheme in Fig. 2.2 all the connections between these components are shown. The chiaro head is combined with the microscope and the probe

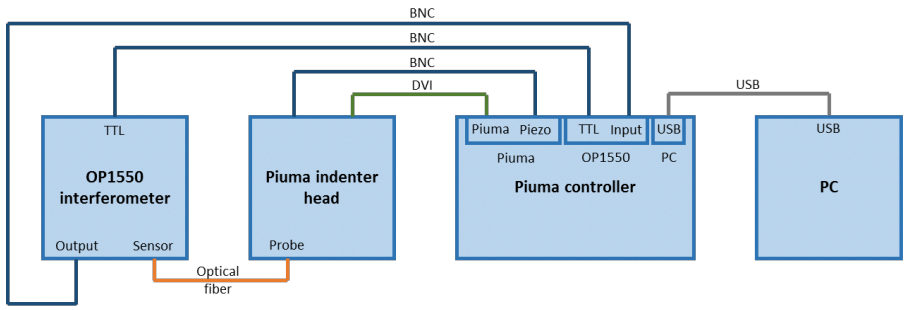

Figure 2.3: Setup connection path.

is positioned on the head and connected to the interferometer. Both the interferometer and the head are connected to the controller: the former is the input signal, the latter one is transmitted to the head to control the probe position.

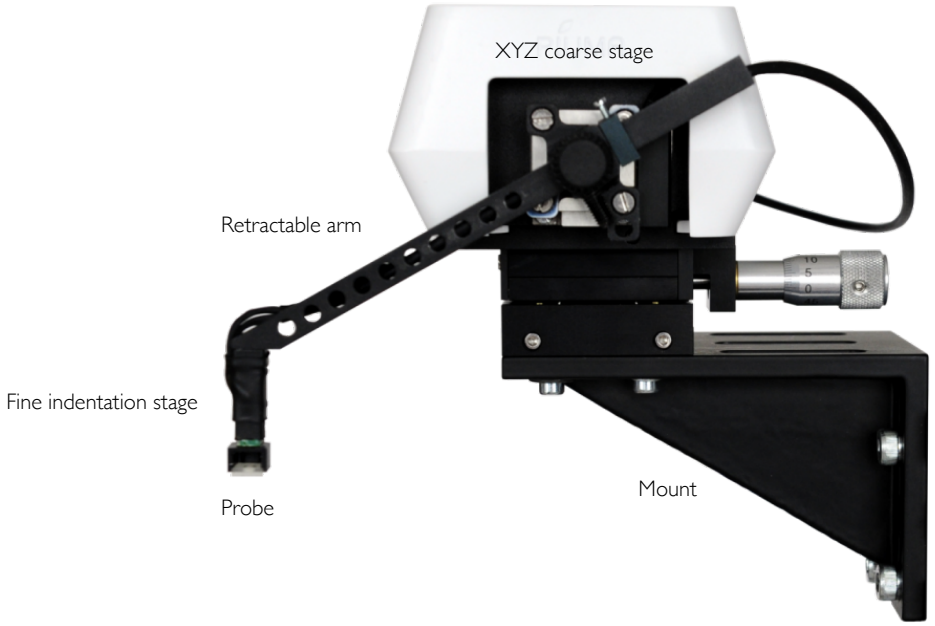

Figure 2.4: The main compoment of the Chiaro head.

In figure 2.4 the head main components are indicated:

- the mount;
- xyz coarse stage;
- a retractable arm;
- a fine indentation stage;
- the probe.

The mount allows the head to be combined with the inverted microscope. Two stages are used for the fine and coarse control of the probe position, while a retractable arm allows to locate the probe on the sample.

The probe, Fig. 2.5 is a one piece optical probe, that consists in an optical fiber, a cantilever and a spherical tip. It is obtained by carving a cantilever on the top of a glass ferrule where also an optical fiber for read-out purposes is hosted, [23]. The deflection of the cantilever is measured via Fabry-Pérot interferometry. A monochromatic light source is connected to a coupler, that is itself connected to the probe.

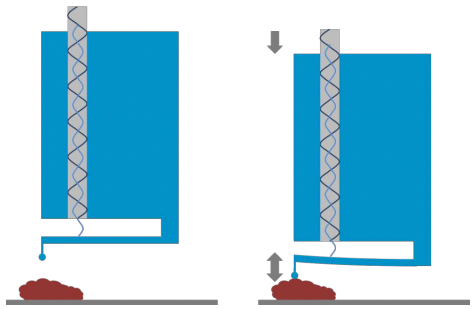

Figure 2.5: Illustration of the probe indenting a cell.

Then a photodiode is used to measure the intensity of the light reflected back from the probe head, resulting from the interference between:

- the ligth reflected at fiber-to-gap interface,
- the ligth reflected at gap-to-cantilever interface,

The amplitude of the interference signal built in such a way has this form:

$$w(d) = w_0 \left[1 + V \cos\left(\frac{4\pi d}{\lambda} + \phi_0 \right) \right] \tag{2.1}$$

where d is the separation between the fiber-to-gap and the gap-to-cantilever interfaces, w_0 is the midpoint interference signal, V is the fringe visibility , λ is the wavelength of the light source and ϕ_0 is a constant phase shift that depends only on the geometry of the cantilever.

2.2.1 Calibrating the system

Two different kind of calibration have to be performed before starting an experiment:

- the calibration of the optical signal,
- the calibration of the geometrical factor.

The first calibration consists in adjusting the interference signal w_0 at the midpoint of the fringe, the quadrature. Generally this can be achieved by tuning the size of the Fabry-Pérot cavity or tuning the wavelength of the light source. In this case it is obtained only through the second solution. The optical calibration is automatically achieved by the interferometer when the probe is dipped in the medium 2.6.

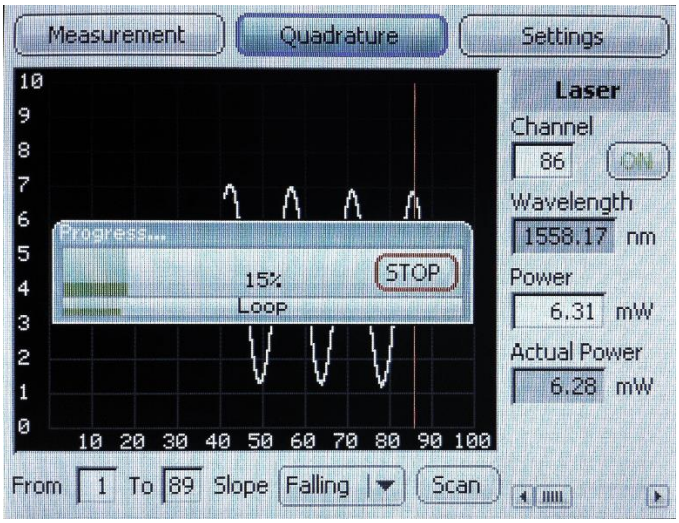

Figure 2.6: Optical calibration performed from the interferometer.

This procedure is necessary because in this way the read-out provides a linear signal both when the cantilever bends backwards during the approach (forward indentation) and also when it bends forward during the retraction of the tip.

The second calibration instead is needed to translate the detector output, that is in volts, to the deflection of the cantilever, that is in nanometers, i. e.

computing the deflection sensitivity. This is accomplished indenting a very stiff sample (usually the bottom of the Petri dish of the sample), so stiff that the indentation depth can be safely considered equal to 0. This means that the indenter tip deflects exaclty the same quantity as the close-loop piezo movement 2.7.

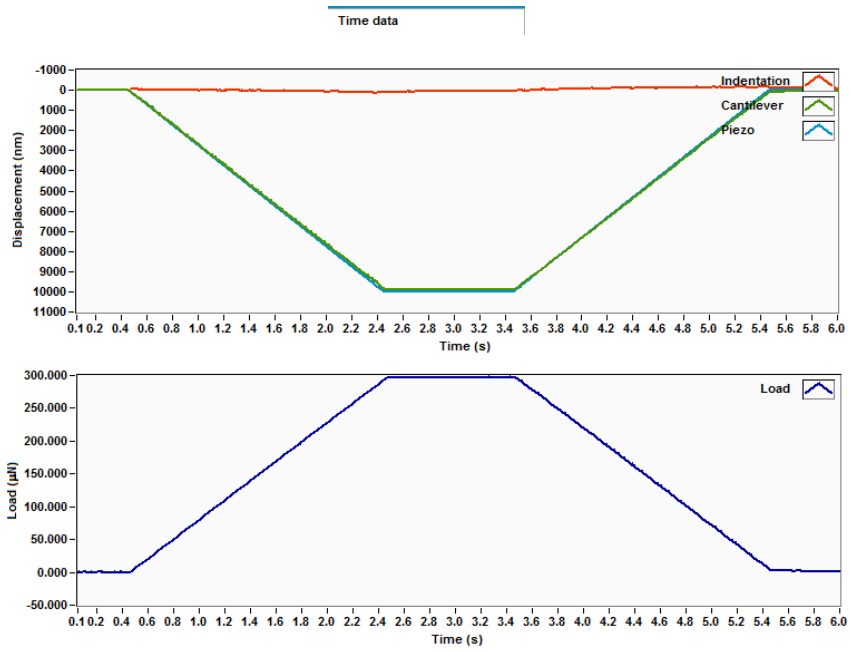

Figure 2.7: Geometrical calibration: the cantilever deflection is equal to the probe displacement.

Then, from the slope of the linear part of the fringe, the deflection sensitivity can be extracted. This applies to the given laser power and the detector gain, therefore this calibration must be performed always after the optical one.

2.3 Probe Selection

Sample of different elasticity can be measured if the appropriate probe is selected. More precisely, in order to address a specific Young's Modulus range, a probe with a specific stiffness and radius must be chosen. In the probe selection chart Fig. 2.8 the range of Young's Modulus that can be addressed depending on the tip radius and stiffness is represented. Given a specific tip stiffness the blue and red lines indicates the upper and lower limits of the Young's modulus range that can be measured. Parallel lines within the limits depend on the tip radius. In experiments concerning the identification of cellular mechanical properties the typical probe stiffness is between 0.05 to $0.5N/m$, and the probe radius is between 3 to $10\mu m$.

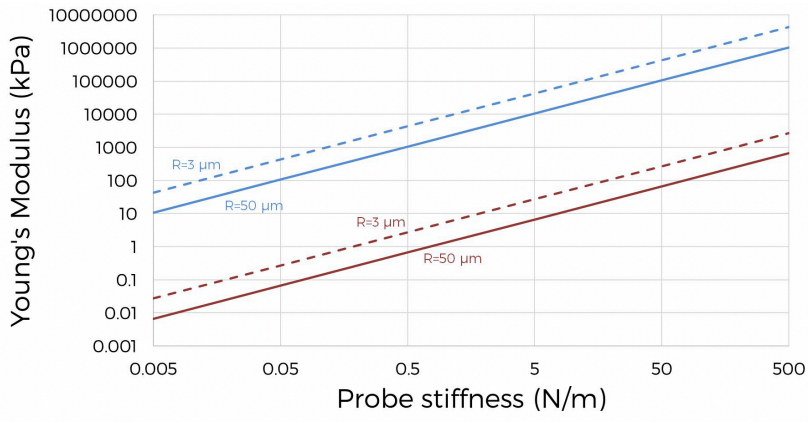

Figure 2.8: Probe selection guide graph [2] : the blue line indicates the upper limit, while the red one indicate the lower.

2.4 Force Displacement Curve

After the calibrations are performed, the experiment can start. In this instrument, as explained before, the only kind of control available is the position control. At the begininnig of the experiment it is possible to define the indentation profile in terms of displacement. The two tunable parameters are the displacement and the time employed for each step. A typical indentation profile is shown in fig. 2.9.

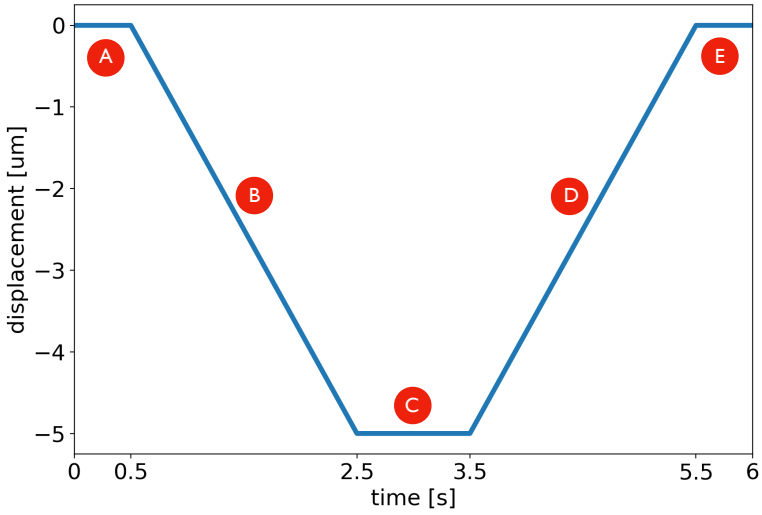

Figure 2.9: Indentation profile settled for a force distance curve.

The probe stands still for $0.5s$ (A), then descends $5\mu m$ with a constant velocity in $2s$ (B), then it stands agan for $1s$ (C). The ascent is specular respect to the descent (D),(E). To stop the approach step, it will be strictly necessary to start the indentation few micrometers above the cell. In this way the cell will be preserved even after the indentation and the measurement will be free from the substrate presence. This is a strict hyphotesis also for the analysis, as it will be explained later.

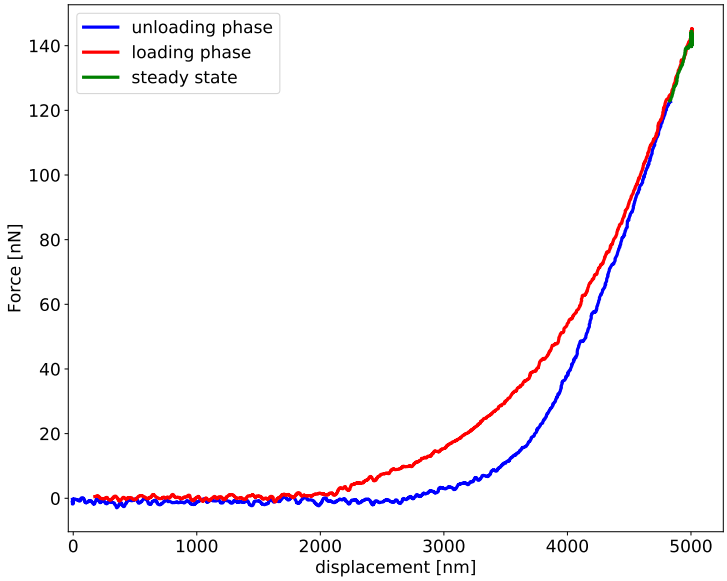

Figure 2.10: Main steps of a force-displacement curve: unloading phase (blue line), loading phase (red line), steady state (green line).

A force displacement curve is therefore composed of 3 main steps: the approach (loading phase), the retract (unloading phase) and a short steady state in between, Fig. 2.10. This instrument allows two different operation modes. The first is more accurate and quicker and consists in performing a single cell measurement. On the other hand it is less effective and few single measurements may be obtained in one experiment. The second is more high-throughput. It consists in choosing a rectangular grid of points in which the instrument automatically performs identations. Step size and number can be chosen in order to personalize the matrix. Obviously this mode results to be less accurate, as it is unlikely all the measurements will be on different cells. However if cells are grouped in large planar clusters this mode provides an high number of reliable measurements in a single experiments.

In this work, because of the limitation of the setup, that doesn't allow to be controlled in force, our focus will be only into the approach. Indeed the

retracting part is dependent on the maximum force reached during the approach, therefore without the possibilty of choosing a maximum force value to start retracting, just the appoaches are comparable between different curves. Here in Fig. 2.11 the approach of a force displacement curve is presented.

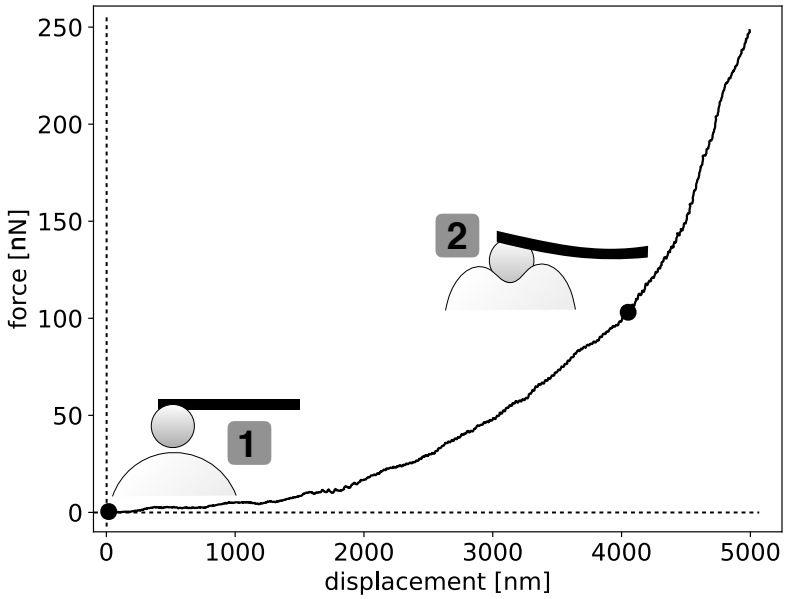

Figure 2.11: Example of a force-displacement curve collected in a classical indentation. The experiment is composed of two main steps: approaching the cell starting from a no contact condition (1), and then indenting the cell, bringing the tip in contact with the sample (2).

The elastic properties of cells can be derived from this measurement. In order to achieve this, a model underlying the nanoindentation measurement has to be assumpted. Many models are used in literature to describe nanoindentation experiments. The choice depends on the phenomenon that it is

intended to describe, but above all the scale at which the phenomenon has to be described.

Chapter 3

Modeling cell mechanics

In order to process the curve to extract a parameter related to the mechanical properties of the sample, it is required to adopt a model to describe the response of the cell to the compression of the indenter. Because results depend on experimental conditions but also on data analysis, choosing the model has a great importance. Several models have been developed depending on the complexity with whom it is necessary to describe the process. In this chapter starting from the simplest model, 3 different approaches will be presented.

3.1 Introduction

Given the outcome of an ordinary nano indentation experiment, a model to describe the indentation process and to derive information about the mechanics of the cell, is needed. The most famous model in literature to describe the response of the cell to the compression of the indenter is the Hertz model. Several models with different levels of complexity have been proposed to perform this task [11], but the simplest approach, based on the Hertzian dynamics still has a primary role in the literature [35].

3.2 Hertz Model

Heinrich Hertz published the work *On the contact of elastic solids* in 1882, [28]. His aim was to describe how optical properties of stacked lenses change under load and the local stress that develops from the contact of the curved surfaces while they deform. It resulted that the deformation depends on the elasticity of the material in contact.

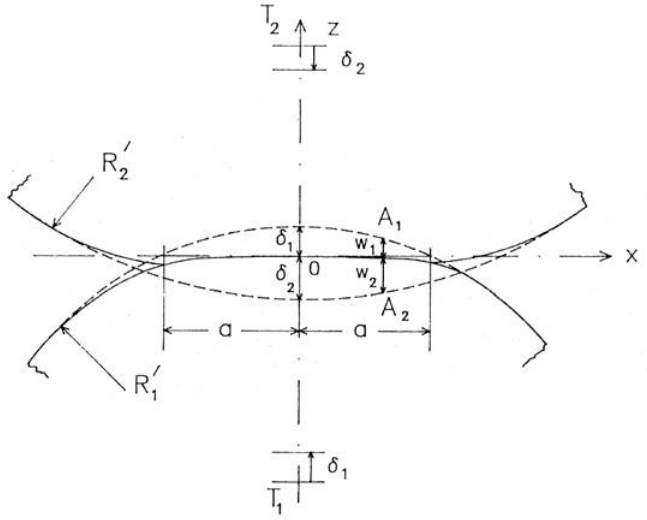

Figure 3.1: *Johnson, K. L. (1985) Contact Mechanics (Cambridge University Press, Cambridge)*

Consider two elastic bodies, with curvature radii R' and R" respectively, in touch at single point 0 before starting deforming, Fig 3.1. In this condition the distance h between two adjacent points A_1 and A_2 can be written as:

$$h = |A_2 - A_1| = \frac{1}{2R'}x^2 + \frac{1}{2R''}y^2 \tag{3.1}$$

If a normal load is applied, the two bodies start compressing. Therefore the distance h will become:

$$h' = h - (\delta_1 + \delta_2) + (\omega_1 + \omega_2), \tag{3.2}$$

where ω_1 and ω_2 are the normal elastic displacements of the surface at A_1 and A_2, while δ_1 and δ_2 are the displacements at the distant point of each

body. If A_1 and A_2 are within the contact area then $h' = 0$ and:

$$\omega_1 + \omega_2 = (\delta_1 + \delta_2) - h. \tag{3.3}$$

Substituting 3.1 in 3.3:

$$\omega_1 + \omega_2 = \delta - \frac{x^2}{2R'} - \frac{y^2}{2R''}, \tag{3.4}$$

with $\delta = \delta_1 + \delta_2 = \omega_1(0) + \omega_2(0)$. Otherwise, if A_1 and A_2 are outside the contaxt area then $h' > 0$ and

$$\omega_1 + \omega_2 > \delta - \frac{x^2}{2R'} - \frac{y^2}{2R''}. \tag{3.5}$$

Force resulting to the surfaces from the trasmission through the contact area includes: a normal load,

$$L = \int_S p dS, \tag{3.6}$$

where p is the normal traction (pressure) and a tangential force Q, of components Q_x and Q_y

$$Q_x = \int_S q_x dS \tag{3.7}$$

$$Q_y = \int_S q_y dS, \tag{3.8}$$

where q_x and q_y are the lateral tractions.

In order to simplify the problem some assumptions are required:

1. strains are small and within elastic limit;
2. each solid can be considered an elastic half space;
3. surfaces are continuos and non conforming;
4. surfaces are frictionless $Q_x = 0$ and $Q_y = 0$.

Then, the elastic displacement at distance r is:

$$\omega(r) = \frac{1 - \nu}{\pi E} \frac{L}{r} \tag{3.9}$$

where E is the Young's modulus and ν the Poisson's ratio. Considering a circular contact point, i. e. $R' = R''$:

- the pressure distribution is

$$p(r) = p_0\sqrt{1 - \frac{r^2}{a^2}}, \tag{3.10}$$

- and the elastic displacement results to be

$$\omega(r) = \frac{1-\nu^2}{E}\frac{\pi p_0}{4a}(2a^2 - r^2), \tag{3.11}$$

where a is the radius of the contact surface.

Considering now the equations 3.11 and 3.4, it has to be true for all r that:

$$\frac{1}{E^*}\frac{\pi p_0}{4a}(2a^2 - r^2) = \delta - \frac{r^2}{2R}, \tag{3.12}$$

where $\frac{1}{E^*} = \frac{1-\nu_1^2}{E_1} + \frac{1-\nu_2^2}{E_2}$.

It follows that:

$$\delta = \frac{\pi a p_0}{2E^*}$$
$$a = \frac{\pi p_0 R}{2E^*}.$$

Therefore the equilibrium load is:

$$L = \int p(r)dS = \int p_0\sqrt{1 - \frac{r^2}{a^2}}dS = \int_0^a p_0\sqrt{1 - \frac{r^2}{a^2}}2\pi r dr = \frac{2}{3}p_0\pi a^2. \tag{3.13}$$

Summarizing and concluding the equation to describe the Hertzian elastic contact are:

- $a = \left(\frac{3LR}{4E^*}\right)^{\frac{1}{3}}$
- $\delta = \frac{a^2}{R} = \left(\frac{9L^2}{16RE^{*^2}}\right)^{\frac{1}{3}}$
- $p_0 = \frac{3L}{2\pi a^2} = \left(\frac{6LE^{*^2}}{\pi^3 R^2}\right)^{\frac{1}{3}}$.

From this equations we can obtain the more interesting force indentation relationship:

$$F = \frac{4}{3}E^*\sqrt{R}\delta^{\frac{3}{2}}, \tag{3.14}$$

where F is the force, R is the radius of the indenter, δ is the indentation depth and $E*$ is related to the elastic properties of the indented object.

Indeed, considering the Hertz model representative for the measurement means describing cell mechanical properties through a single parameter: the Young's modulus. In fact knowing the indenter characteristic parameters, i. e. probe stiffness and radius, the Young's modulus E can be determined. However the measurement resulting from nanoindentation experiments are force-displacement curve. Therefore it is necessary to move from the force-displacement curve to the force-indentation curve, in order to be able to fit the curve with the Hertz model, Fig. 3.2.

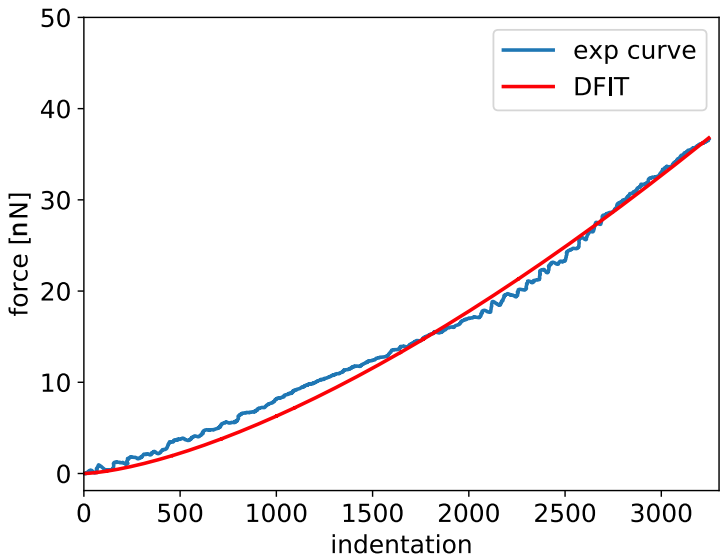

Figure 3.2: Force indentation curve (blue line) fitted with the Hertz model (red line).

The Hertzian model is probably the most used due to its simplicity and even though it requires strict hypothesis, it is still considered a good approximation and a touchstone for cell elasticity measurements. In fact, the intrinsic diversity of single cells inside a population is expected to have a strong impact on the results obtained with a fine grained model, while they are averaged out using a coarse representation. Moreover, the typical repetition rate of single cell experiments (of the order of several 10s of cells per

hour) does not allow to achieve the high throughput required to eventually overcome the biological diversity. The use of the simple Hertz model best suits experimental designs in which the elasticity of single cells is used as a biomarker, whose alterations are associated to changes in the physiological conditions. Although the hypothesis (isotropy, homogeneity and pure elasticity of the sample) are fairly satisfied by a cellular system, this model can still be adopted, but a major caution will be required in the experimental procedure in order to obtain a robust absolute indicator of cell elasticity. Indeed the strong dependence of the result on the experimental condition cannot be ignored [24], [49], that makes it uncomparable unless the protocol from the probe selection to data analysis is almost the same. Nevertheless, when the accent is on the relative change of the parameter, the analysis can be standardized and the variability of the results reduced. In the following, a method is proposed that implements this strategy towards a robust relative evaluation of the mechanical properties.

3.3 Force Integration to Equal Limits (FIEL)

As mentioned before, when an elastic sample is pushed using a perfectly rigid indenter of known geometry, the Hertz model predicts the behavior of the experienced force F as a function of the indentation depth δ which for simple geometries can be written as:

$$F = \gamma E^* \delta^x \tag{3.15}$$

where γ is a factor associated to the geometry of the indenter, E^* is a coefficient related to the mechanical properties of the sample and the exponent x depends primarily on the probe geometry [44], [47]. In the case of a spherical indenter of radius R the relation becomes [33]:

$$F = \frac{4\sqrt{R}}{3} \frac{E}{1-\nu} \delta^{\frac{3}{2}}, \tag{3.16}$$

where E is the Young's modulus and ν is the Poisson ratio of the sample. Fitting this formula to the collected force versus distance curves, it is possible to get an estimate of the Young's modulus for each cell. This procedure, hereinafter called direct fit (DFIT), requires some numerically critical steps, among which the most cumbersome is the identification of the contact point between the tip and the cell, required to convert the displacement in an

indentation. However, while the accent is posed on a relative value of the elastic parameter, to monitor its changes more than measuring its absolute value, a more robust procedure can be introduced, based on the so called Force Integration to Equal Limits (FIEL) method which was proposed for use with the Atomic Force Microscope [18]. In short, the FIEL approach is based on the evaluation of the interaction work, more than the interaction force. Based on the general equation of the Hertz model, the work done while pushing on the substrate up to a defined indentation can be written as:

$$w_0 = \int_0^{\delta_0} F(\delta) d\delta = \int_0^{\delta_0} \gamma E^* \delta^x d\delta = \frac{\gamma E^* \delta_0^{x+1}}{x+1} \tag{3.17}$$

Considering two different force-indentation curves collected with the same probe on two different samples (or different part of the same sample), the ratio of the corresponding works can be written as:

$$\frac{w_1}{w_2} = \frac{E_1^*}{E_2^*} \left(\frac{\delta_1}{\delta_2} \right)^{x+1} \tag{3.18}$$

Moreover, if we limit the integral to a region up to the same force, so that

$$F_1 \delta_1 = F_2 \delta_2 = F_0 \tag{3.19}$$

We can obtain a second equation:

$$\gamma E_1^* \delta_1^x = \gamma E_2^* \delta_2^x \Rightarrow \left(\frac{\delta_1}{\delta_2} \right)^x = \frac{E_2^*}{E_1^*} \tag{3.20}$$

Substituting this equation in the one for the ratio of works, we finally get:

$$\frac{w_1}{w_2} = \frac{E_1^*}{E_2^*} \left(\frac{\delta_1}{\delta_2} \right)^{x+1} = \frac{E_1^*}{E_2^*} \left(\frac{E_2^*}{E_1^*} \right)^{\frac{x+1}{x}} = \left(\frac{E_2^*}{E_1^*} \right)^{\frac{1}{x}} \tag{3.21}$$

Which finally leads to:

$$E_r = \frac{E_2^*}{E_1^*} = \left(\frac{w_1}{w_2} \right)^x \tag{3.22}$$

In which we see that if all the curves are collected with the same probe, the relative stiffness E_r can be simply calculated from the ratio of the integrals up to a defined value of maximum force, Fig. 3.3.

It is clear then an absolute value, if needed, can be achieved also in this case, comparing the sample with one of known stiffness.

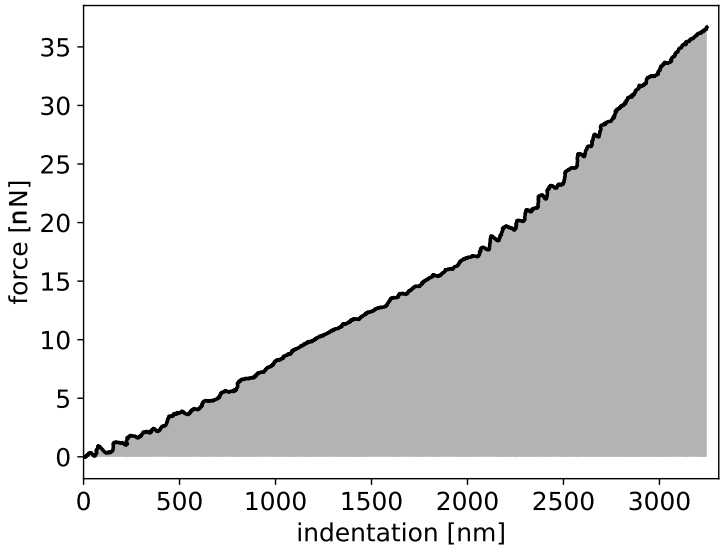

Figure 3.3: Force indentation curve: the area below the curve is the work to compute in the Fiel algorithm.

3.4 Elastography

So far both the methods presented result in one parameter, relative or absolute. However this can not be always enough. A step forward is trying to derive some more information about cell mechanics, specifically if more than one component of the cell can be identified through the force indentation curves.

Consider to segment the force identation curve in N segments and focus on the i-th segment, from δ_i to δ_{i+1}, Fig. 3.4. The work $w_{i,i+1}$ for this segment will be:

$$w_{i,i+1} = \int_{\delta_i}^{\delta_{i+1}} \gamma \frac{\sqrt{R}}{1-\nu} E_{i,i+1} \delta^x d\delta = \frac{\gamma}{1+x} \frac{\sqrt{R}}{1-\nu} E_{i,i+1} (\delta_{i+1}^{x+1} - \delta_i^{x+1}).$$

The work $w_{i-1,i}$ of thr previous segment will be then:

$$w_{i-1,i} = \frac{\gamma}{x+1} \frac{\sqrt{R}}{1-\nu} E_{i-1,i} (\delta_i^{x+1} - \delta_{i-1}^{x+1}).$$

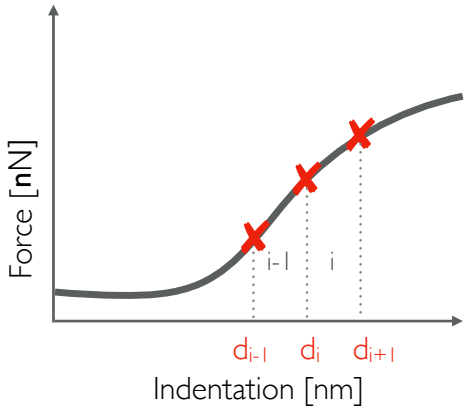

Figure 3.4: Force indentation curve segmented: segments from δ_{i-1} to δ_i and from δ_i to δ_{i+1}.

Then computing the ratio between these two terms we get:

$$\frac{w_{i,i+1}}{w_{i-1,i}} = \frac{E_{i,i+1}}{E_{i-1,i}} \cdot \frac{(\delta_{i+1}^{x+1} - \delta_i^{x+1})}{(\delta_i^{x+1} - \delta_{i-1}^{x+1})}.$$

In the hyphotesis of a uniform segmentation, i. e. choosing a costant indentation step:

$$\delta_0 = 0,\ \delta_1 = \delta,\ \delta_2 = 2 \cdot \delta \ \ldots\ \delta_i = i \cdot \delta$$
$$\text{for } \ i = 0, 1, \ldots, N$$

the equation 3.4 becomes:

$$\frac{w_{i,i+1}}{w_{i-1,i}} = \frac{E_{i,i+1}}{E_{i-1,i}} \cdot \frac{((i+1)^{x+1} \cdot \delta^{x+1} - i^{x+1} \cdot \delta^{x+1})}{(i^{x+1} \cdot \delta^{x+1} - (i-1)^{x+1} \cdot \delta^{x+1})}.$$

We obtain that:

$$E_{i,i+1} = E_{i-1,i} \cdot \frac{w_{i,i+1}}{w_{i-1,i}} \cdot \frac{(i^{x+1} \cdot \delta^{x+1} - (i-1)^{x+1} \cdot \delta^{x+1})}{((i+1)^{x+1} \cdot \delta^{x+1} - i^{x+1} \cdot \delta^{x+1})} = \tag{3.23}$$

$$= E_{i-1,i} \cdot \frac{w_{i,i+1}}{w_{i-1,i}} \cdot \frac{(i^{x+1} - (i-1)^{x+1})}{((i+1)^{x+1} - i^{x+1})}. \tag{3.24}$$

With this equation 3.23 it is possible to compute the elasticity of a segment, by knowing the elasiticity of the previous segment and the ratio between the work of the two segments. Therefore, knowing the elasticity of the

initial segment it is possible to compute the elasticity of all the segments of the curve. One possibility, if the absolute value is needed, would be to fit the inital segment with the Hertz model to derive the Young's modulus. The initial segment, because of its vicinity to the contact point, is often noisy, and a correct fitting can not be achieved. For this reason we computed the equation with respect to a general segment from 0 to δ_i, that if large enough could allow a reliable fitting. In this way the elasticity $E_{0,i}$ of this general portion of the curve, from 0 to δ_i, is computed fitting it with the Hertz model.

Then it can be computed:

- $$w_{0,i} = \int_0^{\delta_i} \gamma \frac{\sqrt{R}}{1-\nu} E_{0,i} \delta^x d\delta = \frac{\gamma}{x+1} \frac{\sqrt{R}}{1-\nu} E_{0,i} \delta_i^{x+1};$$
- $$w_{i-1,i} = \int_{\delta_{i-1}}^{\delta_i} \gamma \frac{\sqrt{R}}{1-\nu} E_{i-1,i} \delta^x d\delta = \frac{\gamma}{x+1} \frac{\sqrt{R}}{1-\nu} E_{i-1,i} (\delta_i^{x+1} - \delta_{i-1}^{x+1});$$
- $$w_{i,i+1} = \int_{\delta_i}^{\delta_{i+1}} \gamma \frac{\sqrt{R}}{1-\nu} E_{i,i+1} \delta^x d\delta = \frac{\gamma}{x+1} \frac{\sqrt{R}}{1-\nu} E_{i,i+1} (\delta_{i+1}^{x+1} - \delta_i^{x+1}).$$

Computing the ratio between the segment $0, i$ and the segment $i-1, i$ we get that:

$$\frac{w_{i-1,i}}{w_{0,i}} = \frac{E_{i-1,i}}{E_{0,i}} \cdot \frac{(\delta_i^{x+1} - \delta_{i-1}^{x+1})}{\delta_i^{x+1}} \tag{3.25}$$

and so the elasticity:

$$E_{i-1,i} = \frac{w_{i-1,i}}{w_{0,i}} \cdot E_{0,i} \cdot \frac{i^{x+1} \cdot \delta^{x+1}}{(i^{x+1} \cdot \delta^{x+1} - (i-1)^{x+1} \cdot \delta^{x+1})} = \tag{3.26}$$

$$= \frac{w_{i-1,i}}{w_{0,i}} \cdot E_{0,i} \cdot \frac{i^{x+1}}{(i^{x+1} - (i-1)^{x+1})}. \tag{3.27}$$

Therefore to compute the Young's modulus for the preceding steps it is sufficient to apply backwards the relationship derived before:

$$E_{i-2,i-1} = E_{i-1,i} \cdot \frac{w_{i-2,i-1}}{w_{i-1,i}} \cdot \frac{(i^{x+1} - (i-1)^{x+1})}{((i-1)^{x+1} - (i-2)^{x+1})}. \tag{3.28}$$

For the consecutive steps it is possible instead to apply original relationship:

$$E_{i,i+1} = E_{i-1,i} \cdot \frac{w_{i,i+1}}{w_{i-1,i}} \cdot \frac{(i^{x+1} - (i-1)^{x+1})}{((i+1)^{x+1} - i^{x+1})}. \tag{3.29}$$

Let's now rewrite the equations respect to the initial step $i = i_0$, assuming it has been conveniently chosen, Fig. 3.5.

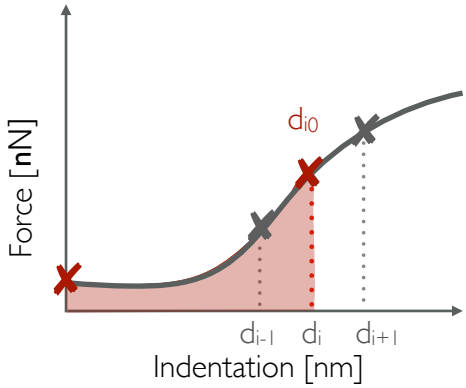

Figure 3.5: Force indentation curve segmented: consider the segment from 0 to δ_{i_0}.

Then we call:

- $E_{i_0} = E_{0,i_0}$;
- $w_{i_0} = w_{0,i_0}$.

Writing the equation 3.26 as a function of i_0 we get:

$$E_{i_0-1,i_0} = \frac{w_{i_0-1,i_0}}{w_{i_0}} \cdot E_{i_0} \cdot \frac{i_0^{x+1}}{(i_0^{x+1} - (i_0-1)^{x+1})}. \tag{3.30}$$

We can derive then E_{i_0-2,i_0-1} combining the previous equation with 3.28:

$$E_{i_0-2,i_0-1} = E_{i_0-1,i_0} \cdot \frac{w_{i_0-2,i_0-1}}{w_{i_0-1,i_0}} \cdot \frac{(i_0^{x+1} - (i_0-1)^{x+1})}{((i_0-1)^{x+1} - (i_0-2)^{x+1})} =$$

$$= E_{i_0} \cdot \frac{\cancel{w_{i_0-1,i_0}}}{w_{i_0}} \cdot \frac{w_{i_0-2,i_0-1}}{\cancel{w_{i_0-1,i_0}}} \cdot \frac{i_0^{x+1}}{\cancel{(i_0^{x+1} - (i_0-1)^{x+1})}} \cdot \frac{\cancel{(i_0^{x+1} - (i_0-1)^{x+1})}}{((i_0-1)^{x+1} - (i_0-2)^{x+1})} =$$

$$= E_{i_0} \cdot \frac{w_{i_0-2,i_0-1}}{w_{i_0}} \cdot \frac{i_0^{x+1}}{((i_0-1)^{x+1} - (i_0-2)^{x+1})}.$$

For a general $i \leq i_0$ the equation becomes:

$$E_{i_0-i,i_0-i+1} = E_{i_0} \cdot \frac{w_{i_0-i,i_0-i+1}}{w_{i_0}} \cdot \frac{i_0^{x+1}}{((i_0-i+1)^{x+1} - (i_0-i)^{x+1})} \qquad \text{per } i \leq i_0 \tag{3.31}$$

Similarly the equation 3.23 for the section from δ_{i_0} to δ_{i_0+1} can be written as:

$$E_{i_0,i_0+1} = E_{i_0-1,i_0} \cdot \frac{w_{i_0,i_0+1}}{w_{i_0-1,i_0}} \cdot \frac{(i_0^{x+1} - (i_0-1)^{x+1})}{((i_0+1)^{x+1} - i_0^{x+1})}. \tag{3.32}$$

Sobstituting 3.26 into 3.32 we get:

$$E_{i_0,i_0+1} = E_{i_0} \cdot \cancel{\frac{w_{i_0-1,i_0}}{w_{i_0}}} \cdot \frac{i_0^{x+1}}{\cancel{(i_0^{x+1} - (i_0-1)^{x+1})}} \cdot \cancel{\frac{w_{i_0,i_0+1}}{w_{i_0-1,i_0}}} \cdot \cancel{\frac{(i_0^{x+1} - (i_0-1)^{x+1})}{((i_0+1)^{x+1} - i_0^{x+1})}} =$$
$$= E_{i_0} \cdot \frac{w_{i_0,i_0+1}}{w_{i_0}} \cdot \frac{i_0^{x+1}}{((i_0+1)^{x+1} - i_0^{x+1})}.$$

For a general step following i_0 the following equation can be written:

$$E_{i_0+i,i_0+i+1} = E_{i_0} \cdot \frac{w_{i_0+i,i_0+i+1}}{w_{i_0}} \cdot \frac{i_0^{x+1}}{((i_0+i+1)^{x+1} - (i_0+i)^{x+1})} \qquad \text{per } i > 0 \tag{3.33}$$

Putting together the equations 3.31 and 3.33 we obtain therefore the general relationship:

$$E_{i_0+i,i_0+i+1} = E_{i_0} \cdot \frac{w_{i_0+i,i_0+i+1}}{w_{i_0}} \cdot \frac{i_0^{x+1}}{((i_0+i+1)^{x+1} - (i_0+i)^{x+1})} \tag{3.34}$$

$$\text{for} \qquad i = -i_0 \ldots, 0, \ldots N - i_0. \tag{3.35}$$

Therefore using this approach, called elastography, is possible to derive elasticity as a function of the indentation depth. If different layers of elasticity exist, as you might think it is true in cell case, choosing the right step, they are found with the elastography.

Assuming the Hertz Model, i.d. $x = \frac{3}{2}$:

- the equation 3.31 becomes:

$$E_{i,i+1} = E_{i-1,i} \cdot \frac{w_{i,i+1}}{w_{i-1,i}} \cdot \frac{(i^{\frac{5}{2}} - (i-1)^{\frac{5}{2}})}{((i+1)^{\frac{5}{2}} - i^{\frac{5}{2}})};$$

- the equation 3.34 becomes:

$$E_{i_0+i,i_0+i+1} = E_{i_0} \cdot \frac{w_{i_0+i,i_0+i+1}}{w_{i_0}} \cdot \frac{i_0^{\frac{5}{2}}}{((i_0+i+1)^{\frac{5}{2}} - (i_0+i)^{\frac{5}{2}})}$$
$$\text{for} \quad i = -i_0 \ldots, 0, \ldots N - i_0.$$

3.5 Comments

In this chapter three approaches have been presented. All the methods require the computation of the force indentation curve. In order to do that, first it is necessary to compute the tip-sample contact point and this results to be one of the most tricky step in the procedure. Indeed there is no analytical formula, no standard procedure that is universally known and used for this computation. As already said before, obtaining results that can be compared requires a specific caution in many operation. Therefore it is clear that because of the strong dependence of the result from the contact point determination, using different empirical procedures introduces errors and leads to uncomparable results. Moving to the FIEL approach, meaning to relative results, avoid all the tricky steps involved in the standard DFIT procedure. Indeed using the same probe, this method results to be independent of the tip-sample contact point. By the way, cells are obviously not homogeneous and the elasticity will not be the same all over the cell. For this reason, facing some biological issues, would be desirable to have more than one parameter to describe the cell. Elastography can help in such a problem providing elasticity as a function of the indentation depth, identifying different indentation layers. In this sense, Elastrography results to be much more informative than the other two methods.

Chapter 4

Procedure optimization

In this chapter the preprocessing required in order to get more reliable results is presented, as well as the accurate steps necessary in the determination of the tip sample contact point. Moreover the influence of the experimental conditions on the results are considered and quantified in order to set an experimental standard procedure to be repeated.

4.1 Introduction

It is of major important keeping in mind that nanoindentation measurements are dependent of several conditions. They result to be dependent on the experimental conditions, such as the temperature, the substrate, the culture medium; they are also dependent on the instrument: on the probe, the loading rate, the indentation depth; they are dependent on the cell states and position and moreover the result depends on data analysis. Therefore it is clear that to generate reliable and comparable results many conditions have to be considered and kept the same. As a result of this, there may be differences among the results in different research groups, even if the problem faced is extacly the same. For example this happened for the mechanical changes during stem cell differentation and also for the elasticity of cancer cells. Therefore it is of major importance designing a procedure that is reliable and robust, such that results are comparable and differences can be highlighted.

4.2 Preprocessing

Once the force displacement curve is collected, in order to derive information about cell mechanics, it is necessary to perform some preprocessing of the measurement. As anticipated the analysis will be performed considering only the approach curve. To be successfully analysed the curve must begin far from the contact point, 4.1. Otherwise it can't be identified and consequently indentation can't be properly computed.

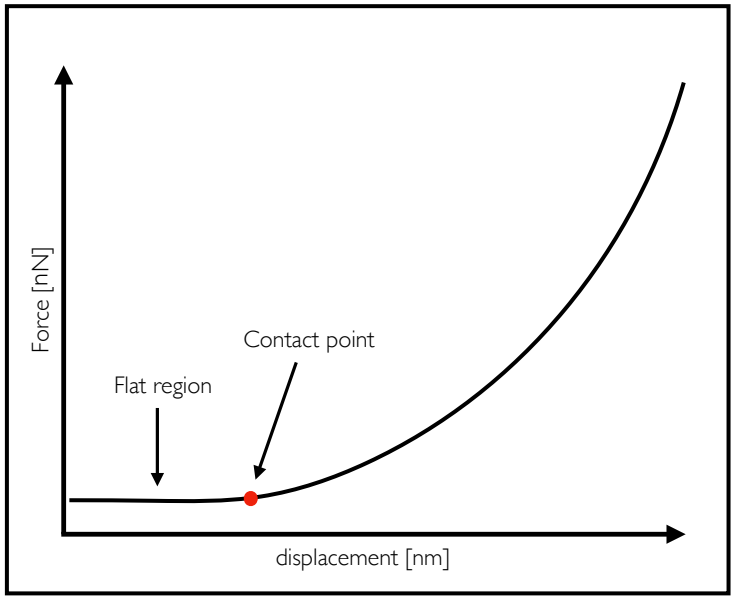

Figure 4.1: Example of an ideal curve: it starts with a flat region so that the contact point can be identified.

The measurement must start not in contact with the cell, this means practically that the curve must start with a flat segment. After it has been assured, using an algorithm, that the curve starts flat, the signal is filtered in order to remove the high frequency noise and make it ready for the computation of the tip-sample contact point. Here in the following the steps of the curve pre-processing.

4.2.1 Pre-processing steps

- The flat region of the force-displacement curve is fitted with a line. The curve is realigned subtracting the line. If the coefficient is higher than a threshold value, typically because it starts already in contact with the cell, the curve is discarded.
- The force-displacement curve is filtered with the Savitzky-Golay filter [48] and its first and second derivatives are computed.

4.3 From force displacement curves to force indentation curves

All the methods presented start from the computation of the force-indentation curve. In order to move from the force-displacement curve to the force indentation curve the tip-sample contact point has to be guess from the curve analysis. This step doesn't result to be trivial and, what is more, a standard procedure for its determination doesn't exist. In the software developed during this project, this point is determined through an empirical algorithm, based on the computation of the force-displacement curve filtered and its derivative. This procedure garantees to determine always a contact point that satisfies the same conditions, therefore the error made, if made, can be considered almost constant. Curves in which the contact point can't be trustfully determined are discarded.

4.3.1 Force-indentation curve computation

- The contact point its determined based on the behaviour of filtered curve and its derivatives.
- Indentation is computed considering force and displacement from the contact point with the equation: $\delta = x_d - \frac{y_d}{\kappa}$.

4.4 DFIT vs FIEL

As explained before DFIT results are affected by the contact point determination. The FIEL method grants reducing the error due to a wrong contact-point estimation. Since the method is based on the computation

of the integral and the integral before the contact point is approximable to zero, the error is reduced. In order to use these methods and obtain comparable results, in both case the force indentation curve is considered till the same force value F_{max}. In the FIEL procedure F_{max} is the maximum force value considered for computing the integral.

4.5 Experimental conditions

Beacuse every link in the chain has to be optimized, different questions about experimental condition and their influece on the final result have been faced. In particular three main experimental condition have been considered:

- the media used during the experiments,
- cell confluency percentage of the sample to indent;
- the duration of the experiment, which must not affect cell mechanical properties.

Once the results are proved to be dependent on these experimental conditions, a standard procedure has to be set, to reduce as possible these dependencies. In the next sections the comparison between different experimental conditions is carried out with the FIEL method. The sample consists in Human Embryonic Kidney cells, an immortalized cell line. Standard protocols and solutions well suited for this cell colture and several measurement of its mechanical properties are available in literature [63], [26]. Cells were seeded in Petri dishes with a diameter of $35mm$. Cell temperature during the experiments was not accurately controlled, however room temperature was always kept around 25°C. Cells were not synchronized before measurements. This leads to a little more variability in the results: data distributions will be less tighter. Nanoindentation experiments were performed with the Chiaro Nanoindenter and one-way ANOVA tests were performed to compute the statistical significance [3].

4.6 Extracellular solution

Every type of cell is cultured within its specific medium, but of course different medium can be used during experiments. HEK cells medium during incubation consists in the Dulbecco's Modified Eagle's Medium (DMEM) high-glucose. Physiological solution has been considered a viable alternative during experiments. This decision is supported by the need of performing experiments of electrophysiology and fluorescence experiments in the future. Indeed the standard solution for these kind of experiments is the physiological solution. HEPES was added to the solution in order to mantain a physiological value of pH. Here the formulation of the physiological solution used:

- $140mM\ NaCl$,
- $5.4mM\ KCl$,
- $10mM\ HEPES$,
- $10mM\ Glucose$,
- $1mM\ MgCl_2$,
- $1.8mM\ CaCl_2$.

The pH has been brought to 7.4 with NaOH. DMEM was replaced with physiological solution 20 minutes before the experiment. The goal was to understand if cell mechanical properties are affected by the medium in which they are bathed.

Nanoindentation experiments were performed on HEK cells sedeed at 30k per ml, both in their culture medium, the DMEM, than in the physiological solution. The experiments were performed after 2 days from the seeding, in order to achieve a higher confluency percentage. In the figure 4.2 the results of this set of experiments are shown. This figure proves that the result depends also on the medium used during the experiment. Therefore, if possible, it has to be the same for every set of experiments, if results should be compared. Otherwise differences due to the medium could be wrongly attributed to other biological differences.

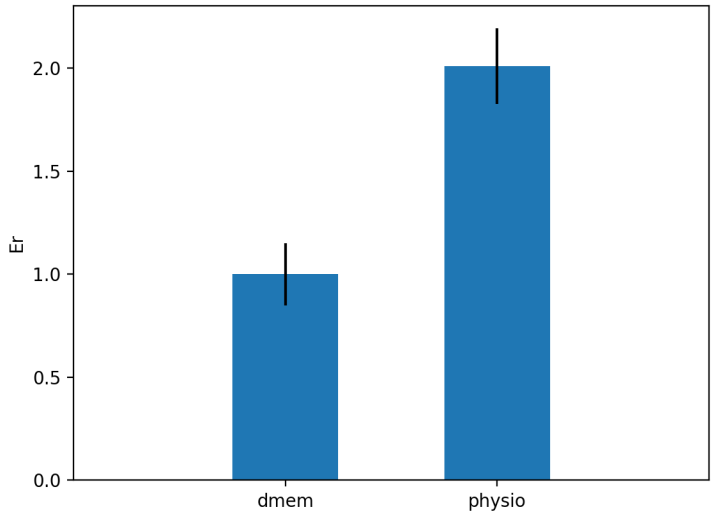

Figure 4.2: Relative elasticity varies depending on the medium: dmem and physiological solution are compared.

4.7 Confluency

One more thing to be considered is the confluency percentage. Are cell mechanical properties affected by the confluency percentage? Cells were seeded at three different concentration: $10k$, $20k$ and $30k$ per ml of medium. Again the experiments were performed with HEK cells after 2 days from the seeding. Cells reached in 2 days a different confluency percentage, without forming a whole uninterrupted monolayer. Results are shown in Fig. 4.3. Indeed mechanical properties depends on the confluency percentage. Relative elasticity appears to increase, increasing the concentration. A significative difference exists between $10k$ and $20k$ and also between $10k$ and $30k$. However there is not a significative difference between the last two conditions, $20k$ and $30k$, suggesting that elasticity is more stable at higher confluency percentage. It was decided to use always the higher concentration, $30k$. The

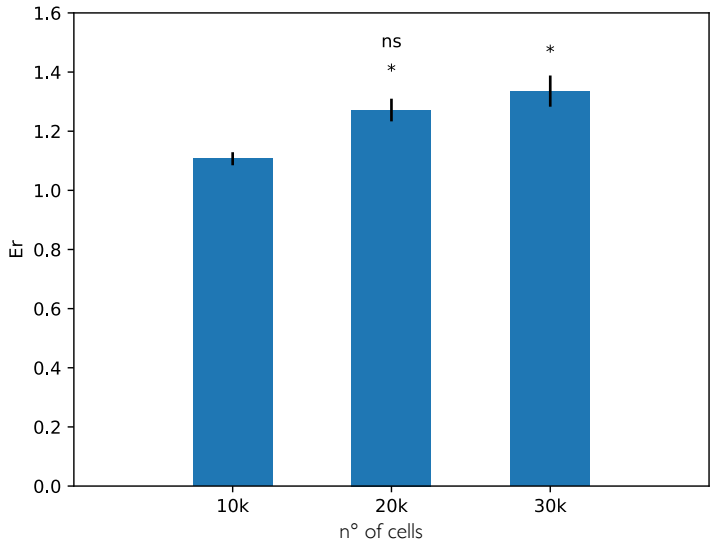

Figure 4.3: Relative elasticity varies depending on cell number: differences between $10k$ and $20k$ and between $10k$ and $30k$ are significative, instead differences $20k$ and $30k$ are not.

reasons are a higher stability of the mechanical properties at higher concen-

tration and the possibility to exploit the automatic matrix measurement, resulting in a higher number of curves per experiment. Therefore results won't be affected by the confluecy percentage.

4.8 Experiment duration

Let's consider now the experiment duration. Results can be compared if the sample deterioration has not affected yet the measures. Indeed a long stay outside the incubator, can lead to cellular distress signs, as blebbs and detachment, and even to death. Experiments were performed with HEK cells seeded with a concentration of $30k$ per ml after 2 days from seeding, in physiological solution. Indentations are compared depending on the min-

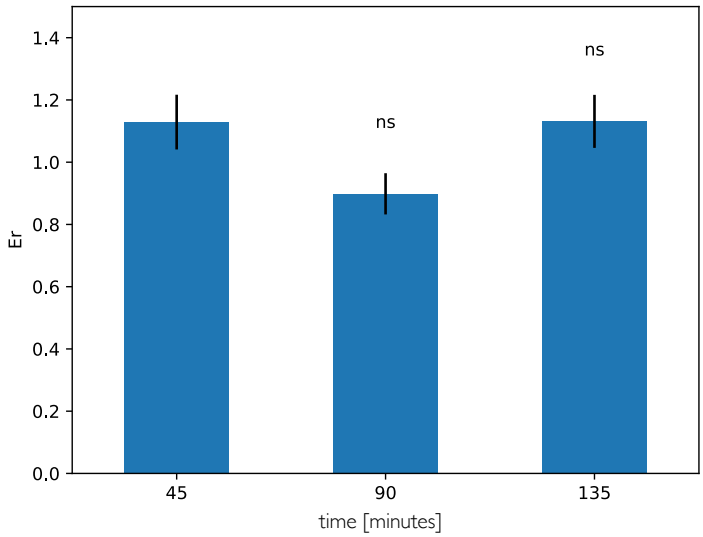

Figure 4.4: Relative elasticity doesn't vary depending on the experiment duration

utes have passed since the experiment started. There is not a significative difference depending on time as shown in Fig. 4.4. This leaded to set the duration of the experiment to a maximum of 2 hours.

4.9 Conclusion

It is true that results in nanoindentation experiments depend on many factors and conditions. In order to obtain comparable results it is necessary to have a great accuracy carrying out the experiments, choosing the experimental conditions and designing the algorithms. However because nanoindentation experiments do not follow a standard protocol, every *absolute* result is hardly comparable within different research groups. Anyway if experiments are carefully planned and experimental conditions are kept constant, then *relative* results are comparable.

Chapter 5

Simulations

The elastography theory is applied to obtain Stiffness vs Indentation depth curves. The shape of the computed elastography curves resembles the stiffness curve obtained indenting a bilayer of two different stiffnesses. This observation led to design two different procedures based on the relationships presented in the model section 3.4, in order to derive the stiffness curve and its representative parameters. All the procedures, included FIEL and DFIT, were tested in simulation to prove their effectiveness. The influence on the result of the indentation step and the noise is considered.

5.1 Elastography: from the experimental curves to the bilayer model

Once the theory of the elastography has been implemented, experimental curves were computed from experimental force-indentation curves. HEK cells are used as sample for nanoindentation experiments. The indentation step was set to $30nm$ and $E_{i_0} = E_{0,i_0}$ (3.30) was computed from the force indentation curves considering as maximum force $50nN$. The results are stiffness curves as a function of the indentation depth, Fig. 5.1. This behaviour of the curve suggests that there are at least two different values of elasticity hidden in the force indentation-curves: one external, stiffer and one internal, softer. This particular curve shape already exists in literature, [64].

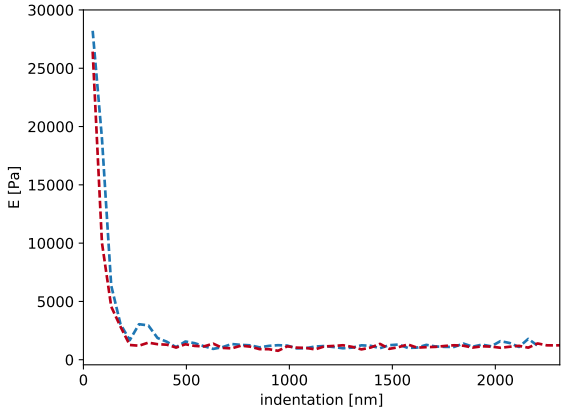

Figure 5.1: Examples of experimental stiffness curves depending on the indentation depth.

It represents the stiffness measured in a bilayer indentation 5.2. The stiffness representative equation of the bilayer is:

$$E(\delta) = E_b + (E_0 - E_b) \exp^{-\frac{\sqrt{R\delta}}{d_{0b}}} . \tag{5.1}$$

It is a function of the indentation depth and it is described by three parameters:

- E_0, the stiffness of the external layer;
- E_b, the stiffness of the internal layer;
- d_{0b}, the thickness of the external layer.

Therefore with the Elastography the information about cell mechanics available to infer it is much more respect to the previous methods. Indeed if the bilayer model is supposed to be representative, because it resembles the elastography curve, then the method allows to distingush inside the cell at least two different layers of elasticity. These two layers could be related to cellular inner components with different elasticity. Speculations lead us to think that the external stiffness layer could be related to the actin cortex stiffness and the internal stiffness layer to the other inner components of the cell, nucleus included.

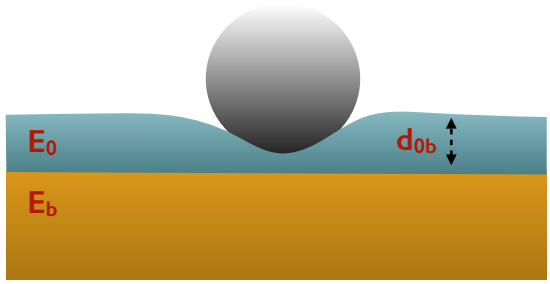

Figure 5.2:

5.2 Elastography: Absolute and Relative

The observation that the elastography curve could highlight a bilayer model, hidden in the force indentation curve, led to design two different procedures. The first presented is based on the second relationship derived in section 3.4:

$$E_{i_0+i,i_0+i+1} = E_{i_0} \cdot \frac{w_{i_0+i,i_0+i+1}}{w_{i_0}} \cdot \frac{i_0^{\frac{5}{2}}}{((i_0+i+1)^{\frac{5}{2}} - (i_0+i)^{\frac{5}{2}})} \tag{5.2}$$

$$\text{for} \quad i = -i_0 \ldots, 0, \ldots N - i_0. \tag{5.3}$$

Assuming to choose a initial segment from 0 to δ_{i_0}, the segment stiffness E_{i_0} can be computed fitting with the Hertz model the force indentation curve til δ_{i_0}. Then the stiffness of each segment can be computed knowing E_{i_0} and computing the work related to the segment and w_{i_0}, as shown in the equation 5.2. Now that the elastrography curve has been computed it can be fitted with the bilayer model in order to find the three parameters cited before. This procedure is named *Absolute* elastography. Another approach instead consists in exploting the first relationship found in the elastography theory:

$$E_{i,i+1} = E_{i-1,i} \cdot \frac{w_{i,i+1}}{w_{i-1,i}} \cdot \frac{(i^{\frac{5}{2}} - (i-1)^{\frac{5}{2}})}{((i+1)^{\frac{5}{2}} - i^{\frac{5}{2}})}. \tag{5.4}$$

With this equation it is possible to build a *relative* stiffness versus indentation depth curve. Then this curve can be still fitted with the bilayer model:

$$E_{rel}(\delta) = E_{br} + (E_{0r} - E_{br})e^{-\frac{\sqrt{R\delta}}{d_{0b}}}, \tag{5.5}$$

where E_{br} is the relative stiffness of the internal layer, E_{0r} is the relative stiffness of the external layer, while d_{0b} is the effective thickness of the external layer. The absolute elasticity could be then computed knowing the *scaling factor*r κ, such that:

$$E_{abs}(\delta) = \kappa E_{rel}(\delta). \tag{5.6}$$

It is known that the force indentation curve for the bilayer indentation has this form:

$$F(\delta) = \frac{4\sqrt{R}E(\delta)}{3(1-\rho)}\delta^{\frac{3}{2}} = \frac{4\sqrt{R}(E_b + (E_0 - E_b)\exp^{-\frac{\sqrt{R\delta}}{d_{0b}}})}{3(1-\rho)}\delta^{\frac{3}{2}}. \tag{5.7}$$

Therefore to find the scaling factor κ, it is possible to fit the force-indentation curve with 5.7 but replacing $E(\delta)$ with $\kappa E_{rel}(\delta)$:

$$F(\delta) = \frac{4\sqrt{R}\kappa E_{rel}(\delta)}{3(1-\rho)}\delta^{\frac{3}{2}} = \frac{4\sqrt{R}\kappa(E_{br} + (E_{0r} - E_{br})\exp^{-\frac{\sqrt{R\delta}}{d_{0b}}})}{3(1-\rho)}\delta^{\frac{3}{2}}. \tag{5.8}$$

In the fitting procedure κ is unknown, while E_{0r}, E_{br} and d_{0b} are the result of the first fit with the relative elastography curve. Once κ has been found, E_0 and E_b are obtained simply:

- $E_0 = \kappa E_{0r}$;
- $E_b = \kappa E_{br}$.

This procedure is named *Relative* elastography.

5.3 Simulation

To prove in a simulation environment if all the methods presented could effectively indentify the true value of the parameters, test force-indentation curves were generated via software using equation 5.7. The curves were generated considering different values of the parameters. Three different case have been considered:

- $E_0 > E_b$, stiffer external layer;
- $E_0 < E_b$, stiffer internal layer;
- $E_0 = E_b$, the single layer case.

The maximum force considered is $50nN$ for DFIT and Fiel, and the indentation corresponding to $50nN$ in force, is considered as δ_{i_0} for the absolute elastography. The indentation step considered for all this simulations is $5nm$.

5.4 Stiffer external layer

The first set of simulations presented regards the case of a stiffer external layer $E_0 > E_b$. Results for 3 different sets of parameters are shown:

p1. $E_0 = 30kPa, E_0 = 3kPa, d_{0b} = 500nm$;

p2. $E_0 = 10kPa, E_0 = 3kPa, d_{0b} = 500nm$.

p3. $E_0 = 10kPa, E_0 = 6kPa, d_{0b} = 500nm$.

Both the DFIT and FIEL procedures were applied to the force indentation curve to test the behaviour of the methods in the presence of a bilayer 5.3 and 5.4. It can be noted that both methods in the case of a bilayer are able to identify just the internal layer. Indeed the red lines, that represents the stiffness found with the standard methods match always the black lines, that represent the true internal layer stiffness, E_b.

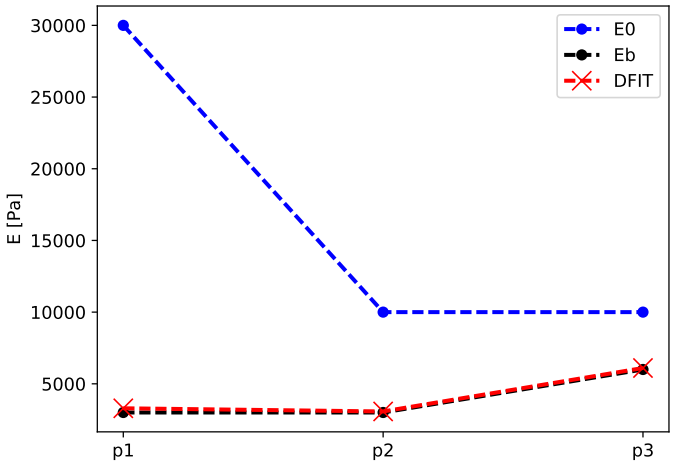

Figure 5.3: When a bilayer exists, the DFIT method identifies just the internal layer stiffness. The blue line represents the external stiffness, the black line the internal stiffness, the red line represents the results obtained with the DFIT algorithm.

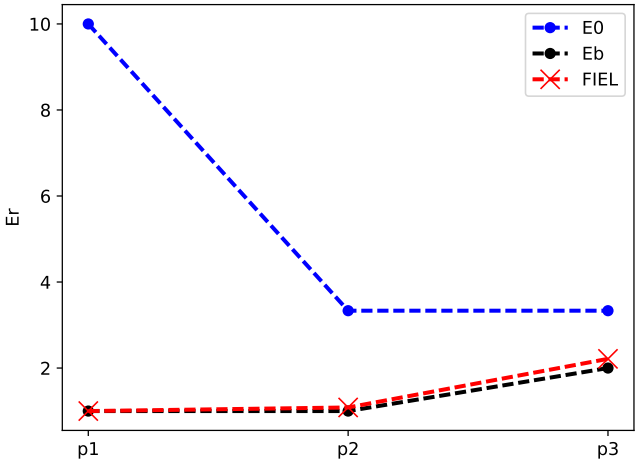

Figure 5.4: When a bilayer exists, the FIEL method identifies just the internal layer stiffness. The blue line represents the external stiffness, the black line the internal stiffness, the red line represents the results obtained with the FIEL algorithm.

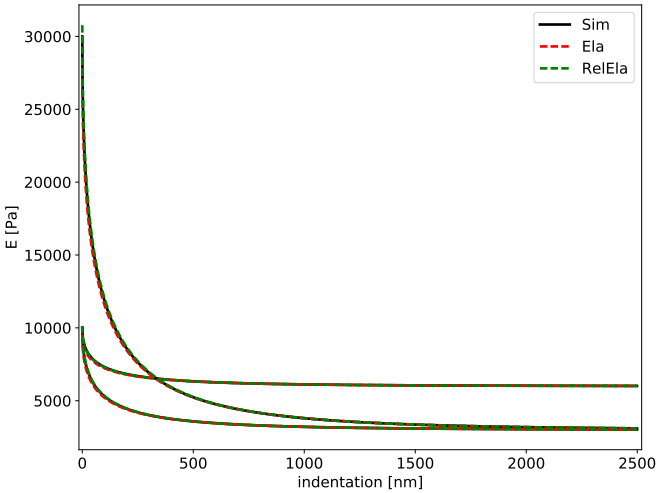

Figure 5.5: Elastography vs Relative elastography curves: both the approaches (red and green lines) succeed in reconstructing the original stiffness curve (black line).

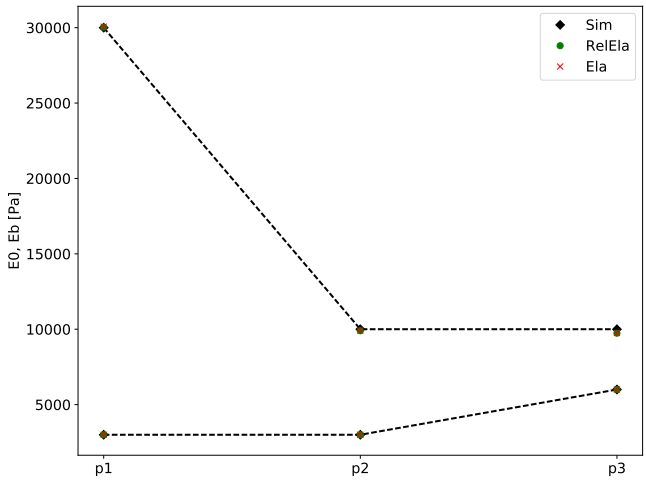

Figure 5.6: External and internal layer stiffness for the 3 sets of parameters.

Instead if the Classic and Relative elastography are applied then the Stiffness vs Indentation depth curve is completely recovered, Fig. 5.5.

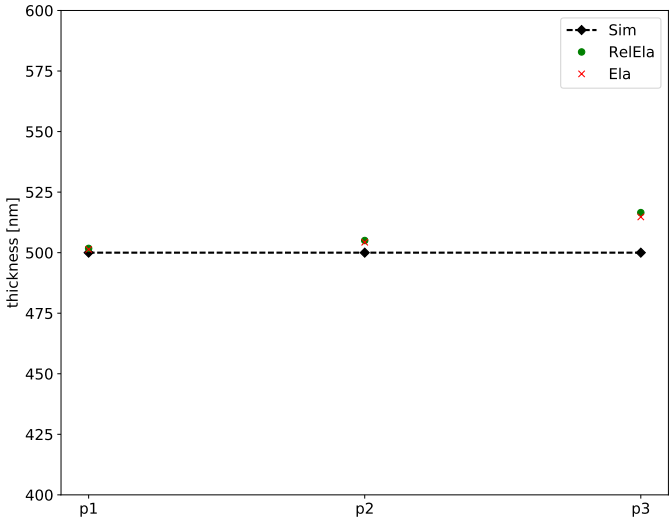

Figure 5.7: Thickness of the external layer for the 3 sets of parameters.

Looking at the parameters in detail Fig. 5.6 and Fig. 5.7, the errors are pretty small and defintely smaller for the relative elastography then for the absolute elastography approach. These small errors depend on the approximation due to the initial segmentation of the curve, therefore they can't be completely cancelled.

5.5 Stiffer internal layer

Let's now consider the case $E_b > E_0$, which means that the internal layer is stiffer than the external. Results are shown for three different sets of parameters:

p1 $E_0 = 3kPa, E_0 = 30kPa, d_{0b} = 500nm$;

p2 $E_0 = 3kPa, E_0 = 10kPa, d_{0b} = 500nm$.

p3 $E_0 = 6kPa, E_0 = 10kPa, d_{0b} = 500nm$.

Again the first results prensented are for the FIEL and DFIT method. As seen before these two methods identify just the internal layer stiffness, even when the external is softer, Fig. 5.8 and Fig. 5.9.

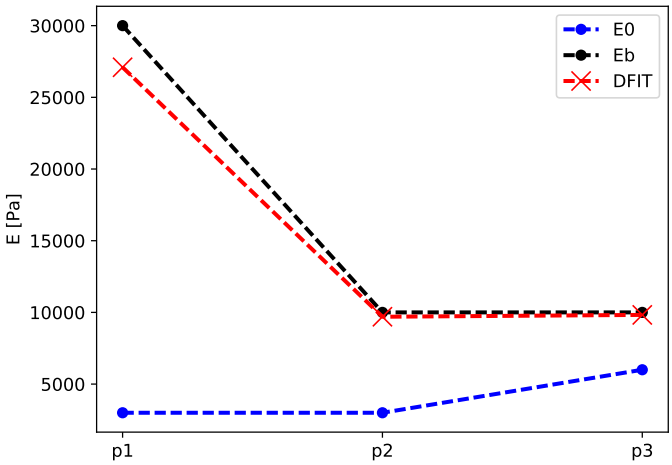

Figure 5.8: When a bilayer exists, the DFIT method identifies just the internal layer stiffness. The blue line represents the external stiffness, the black line the internal stiffness, the red line represents the results obtained with the DFIT algorithm

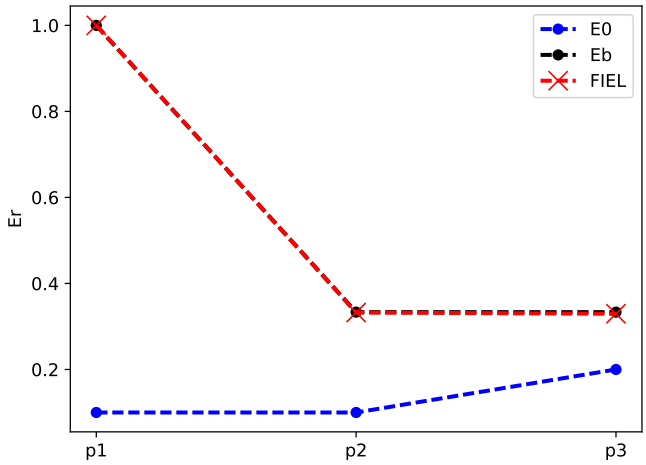

Figure 5.9: When a bilayer exists, the FIEL method identifies just the internal layer stiffness. The blue line represents the external stiffness, the black line the internal stiffness, the red line represents the results obtained with the FIEL algorithm.

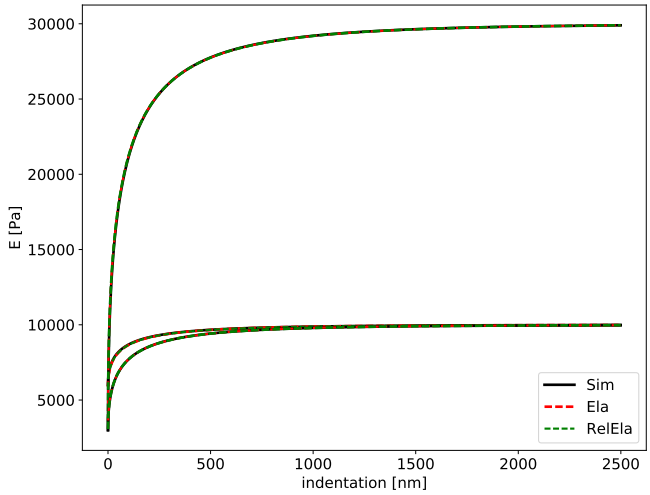

Figure 5.10: Elastography vs Relative elastography curves: both the approaches (red and green lines) succeed in reconstructing the original stiffness curve (black line).

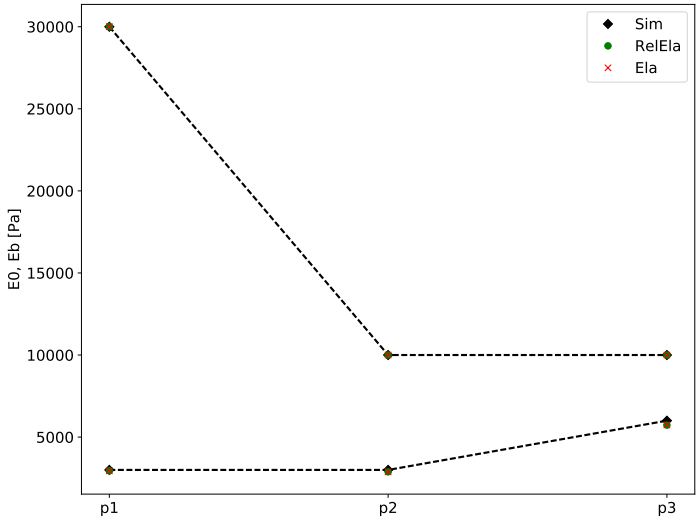

Figure 5.11: Elastography vs Relative elastography: E_0 and E_b.

Something different happens using both the relative and classic elastography. Indeed this two methods allow to precisely reconstruct the shape of the stiffness curve, Fig. 5.10. This allows to recover also the three parameters necessary to describe the bilayer curve 5.11 and Fig. 5.12.

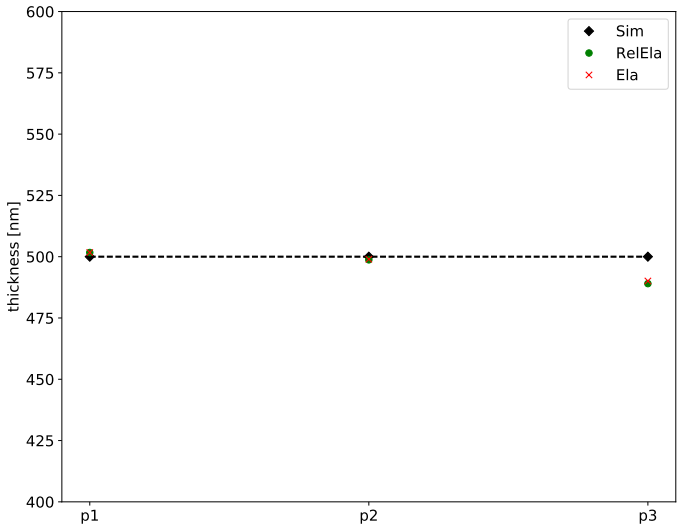

Figure 5.12: Elastography vs Relative elastography: d_{0b} .

5.6 Varying the thickness of the external layer

The methods have been tested varying the internal and external stiffness. However the external layer thickness have been kept constant in all the previous simulations. In this section variations of the external layers are considered for both the case presented, stiffer external layer and stiffer internal layer. First three conditions are considered in the case $E_0 > E_b$:

p1. $E_0 = 30kPa, E_0 = 3kPa, d_{0b} = 300nm$;

p2. $E_0 = 30kPa, E_0 = 3kPa, d_{0b} = 500nm$.

p3. $E_0 = 30kPa, E_0 = 3kPa, d_{0b} = 700nm$.

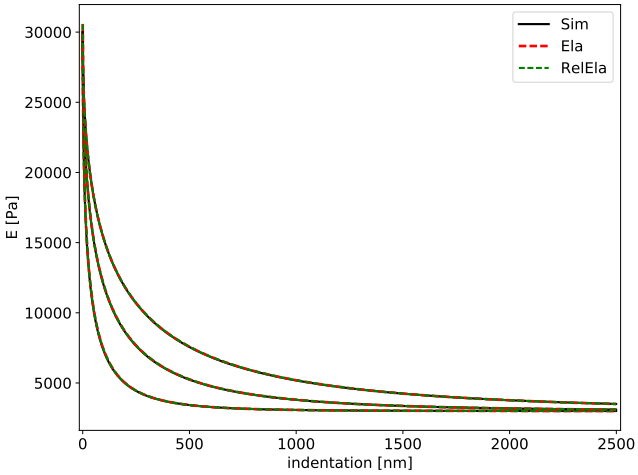

Figure 5.13: Elastography vs Relative elastography varying the thickness d_{0b}:both the approaches (red and green lines) succeed in reconstructing the original stiffness curve (black line).

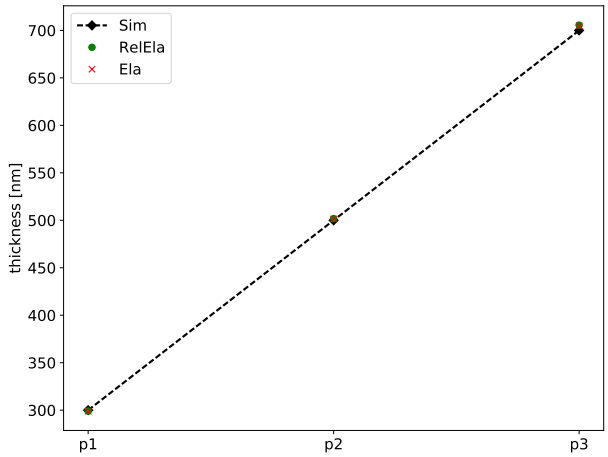

Figure 5.14: Elastography vs Relative elastography varying the thickness d_{0b}.

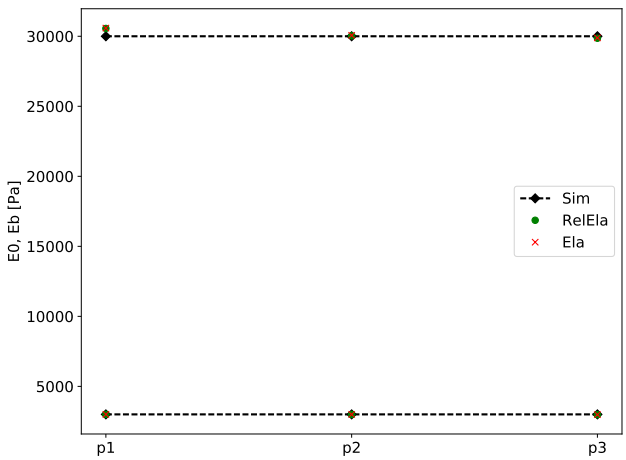

Figure 5.15: Elastography vs Relative elastography varying the thickness d_{0b}: E_b and E_0.

In Fig. 5.13 are presented the elastography curves, in Fig. 5.14 the error on the stiffness parameters, while in Fig. 5.15 the thickness for the three conditions.

The same simulations are performed for $E_b > E_0$:

p4. $E_0 = 3kPa, E_0 = 30kPa, d_{0b} = 300nm$;

p5. $E_0 = 3kPa, E_0 = 30kPa, d_{0b} = 500nm$.

p6. $E_0 = 3kPa, E_0 = 30kPa, d_{0b} = 700nm$.

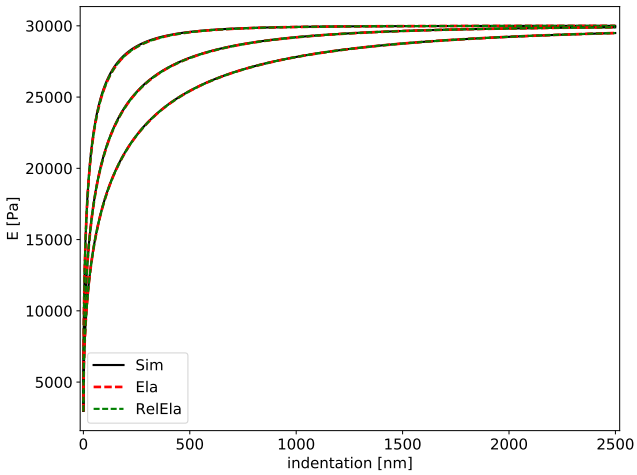

Figure 5.16: Elastography vs Relative elastography varying the thickness d_{0b}: both the approaches (red and green lines) succeed in reconstructing the original stiffness curve (black line).

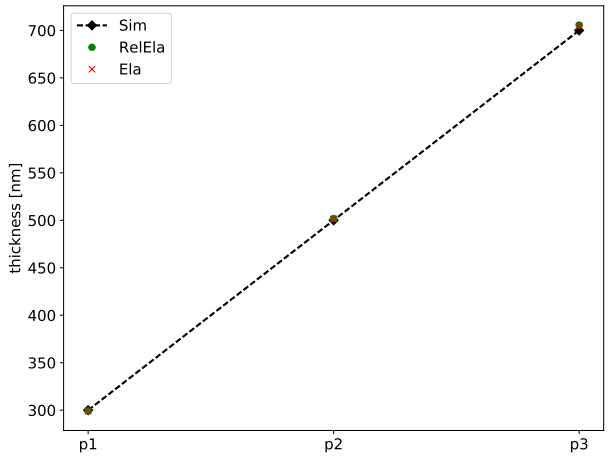

Figure 5.17: Elastography vs Relative elastography varying the thickness d_{0b}.

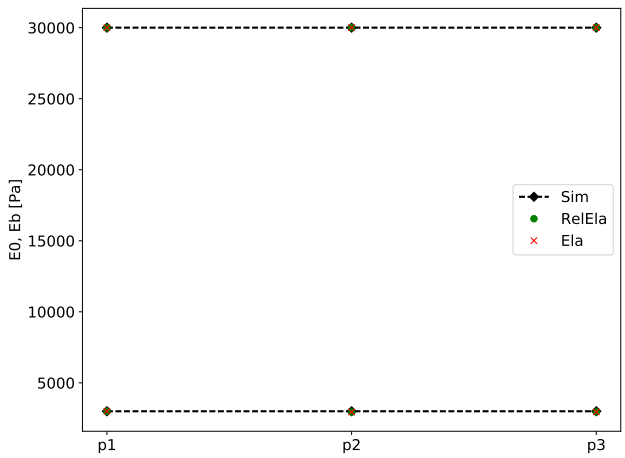

Figure 5.18: Elastography vs Relative elastography varying the thickness d_{0b}: E_b and E_0.

The same good results are obtained for both the conditions and changing the parameters values.

5.7 Single layer

The Elastography was tested also in the single layer case: $E_0 = E_b$. Results are shown for three different elasticity values:

- $E1 = 1kPa$,
- $E2 = 3kPa$,
- $E3 = 10kPa$.

In Fig. 5.19 results for Relative and Classic elastography are presented. Both methods are perfectly able to recover the stiffness true value also in the single layer case.

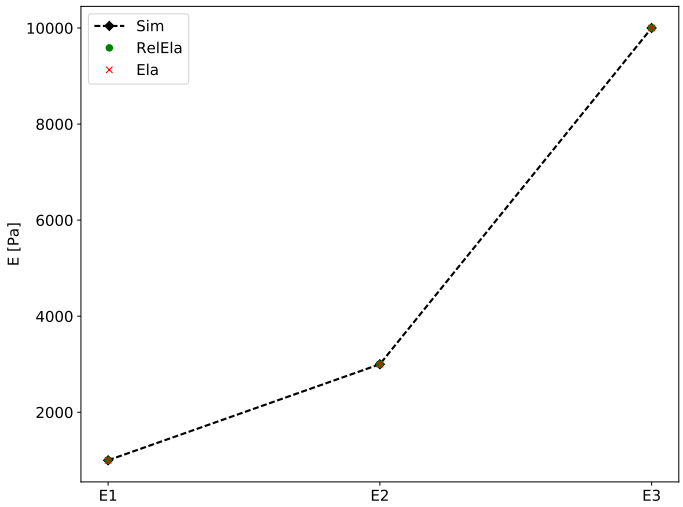

Figure 5.19: Elastography vs Relative elastography for the single layer.

5.8 Varying the indentation step

Another condition has to be considered. The Elastography curve infact results to be dependent on the length of the indentation step. Indeed choosing a different step, the result is averaged on a larger or shorter segment, leading to a different accuracy on the true curve reconstruction. For this reason simulations were performed also varying the indentation step, in order to find the maximum value that can be used, with an acceptable mistake.

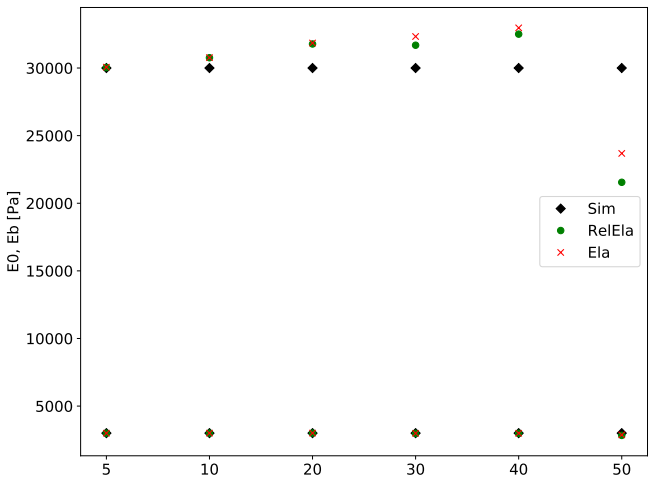

Figure 5.20: Elastography curve varying the indentation step.

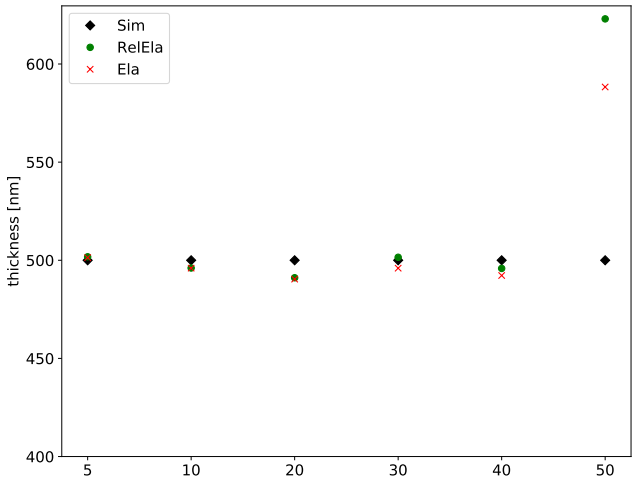

Figure 5.21: Elastography curve varying the indentation step.

In Fig. 5.20 and 5.21 the representative parameters of the bilayer model are presentend, depending on the indentation step length. Values were considered between $5nm$ to $50nm$. Results indicate that using an indentation step of $5nm$ allows to reduce and almost eliminate the error in the parameters determination. The error is considered acceptable till $40nm$, for both parameters. It is notable that the error mainly concerns the determination of the external layer stiffness and thickness, whereas it is practically zero for the internal stiffness layer.

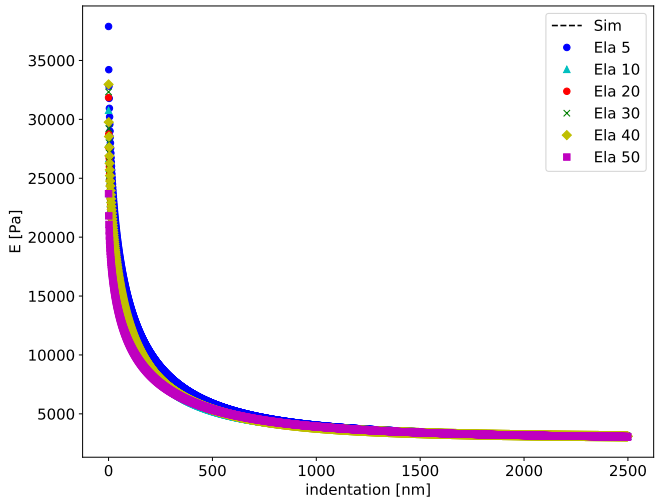

Figure 5.22: Elastography curve varying the indentation step.

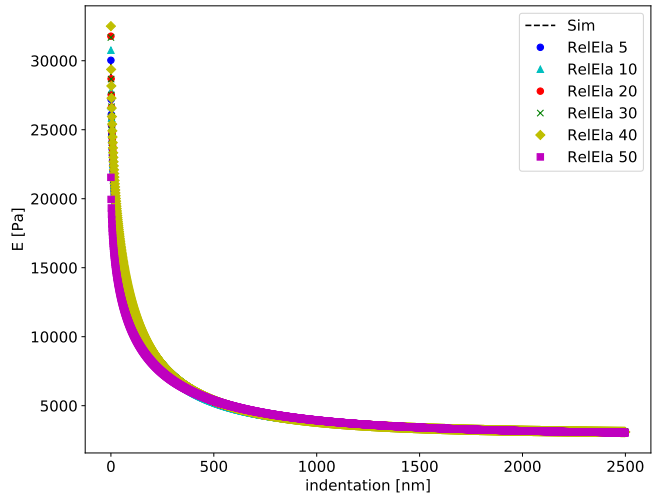

Figure 5.23: Elastography curve varying the indentation step.

5.9 Adding noise

Results depend also on the measurement noise, therefore simulations have to consider this contribution. The indentation step was set to $5nm$. The noise considered is a gaussian white noise with a standard deviation between 0 to $0.5\mu N$, and it was added directly on the force-indentation curve. This can be considered enough, given that the signal is always filtered and smoothed before being processed and that the noise usually involved in these measurement is high frequency noise and easily removed from the curve. Again, both conditions $E_0 > E_b$ and $E_0 < E_b$ are considered. Fig. 5.24 and Fig. 5.25 refer to the first condition, while Fig. 5.26 and Fig. 5.27 refer to the second condition. In both the case the internal layer is slightly affected by the noise, while the other two parameters have acceptable errors til the noise standard deviation reaches $0.5\mu N$.

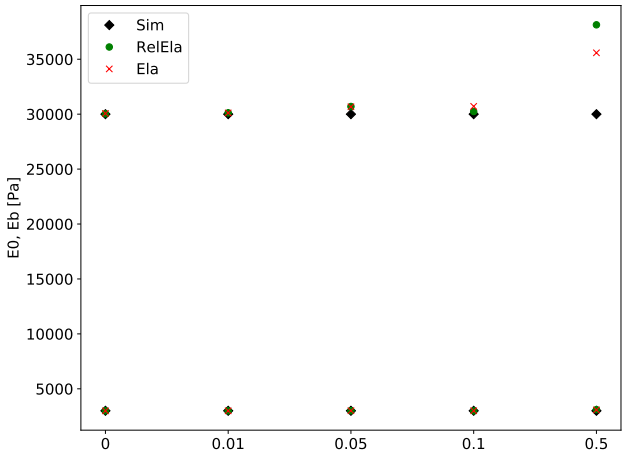

Figure 5.24: Elastography curve with noise: $E_0 > E_b$.

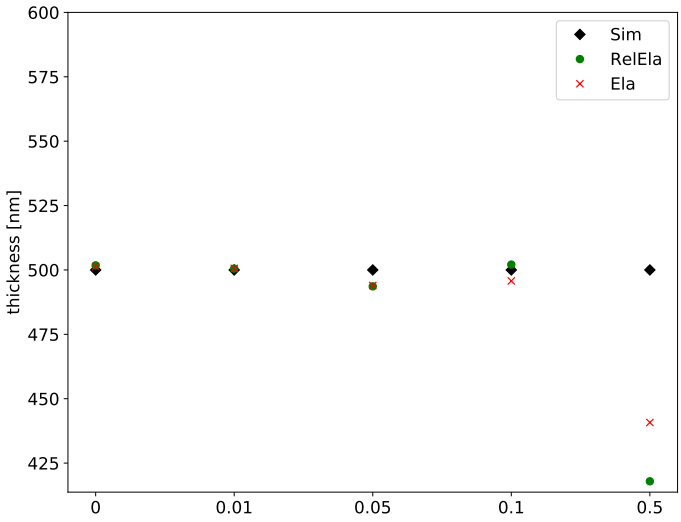

Figure 5.25: Elastography curve with noise: $E_0 > E_b$

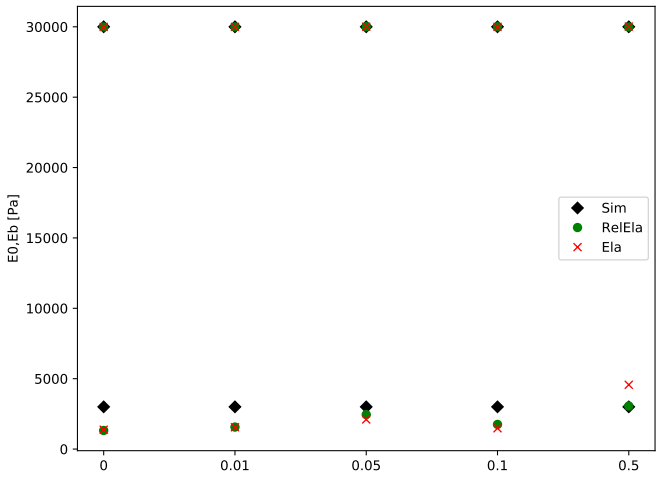

Figure 5.26: Elastography curve with noise: $E_0 < E_b$.

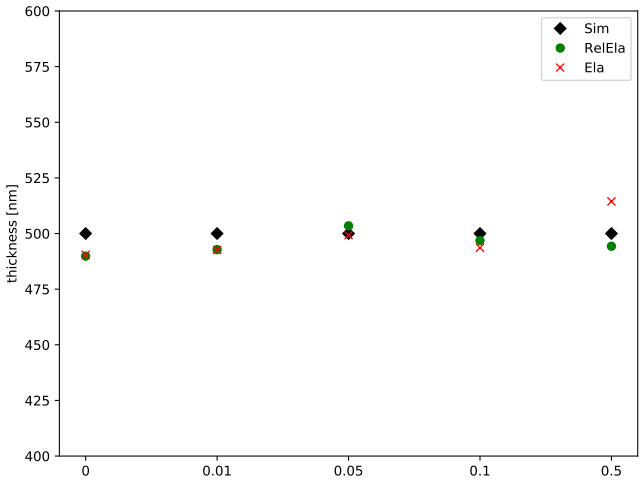

Figure 5.27: Elastography curve with noise: $E_0 < E_b$.

5.10 Conclusion

Simulation showed that Elastography allows to support and increase the information obtained with the standard methods, Fiel and DFIT. Indeed the information obtained with the standard methods is still embedded in the internal layer stiffness, while additional information is obtained in terms of external layer stiffness and thickness. It must be noticed that the elastography doesn't make any a priopri assumption on the model underlying, except that the curve is *locally* approximated with the Hertz model. This means that if the stiffness curve has another shape (three layers, four layers ecc..) it can be recovered through elastography. If it is found that the experimental stiffness curve derived with elastography matches the bilayer ones, then one of the two approaches simulated, the classic and relative, can be applied. Therefore it is important, before applying these procedures, that the elastography curve is observed, to verify if it can be represented with the bilayer model. If this is the case, simulation proved that the classic and relative elastography both are optimal methods to compute the true values of the parameters of the bilayer model. Moreover simulating the system led to identify the optimal condition in order to obtain reasonably accurate results. Infact indentation step has been set its length to $5nm$ and noise simulations have proved that the methods are quite robust to the measurement noise.

Chapter 6

Biological problems

In this chapter all the biological problems faced using the methods already presented in the previous chapters are explained and the results are shown.

6.1 Introduction

All the methods presented and tested in the previous chapters are now applied to real biological problems. These projects are the result of different collaboration with biological and medical laboratories. In every project, nanoindentation measurement were performed on different biological systems. The project regarding FaO cells was carried out in collaboration with the Department of Earth, Environment and Life Sciences (DISTAV) of the University of Genova. The project concerning the a1 cells was the result of a collaboration with the Center of Excellence for Biomedical Research (CEBR) of Genova. The project involving Piezo1 cells was carried out in collaboration with the Victor Chang Cardiac Research Institute of Sydney.

6.2 Human Fetal Osteoblast

The Human Fetal Osteoblastic cells (hFOB) are an immortalized cell line used as a model system for studying human osteoblast differentiation, osteoblast physiology, and hormonal, growth factor, and other cytokine effects on osteoblast function and differentiation.

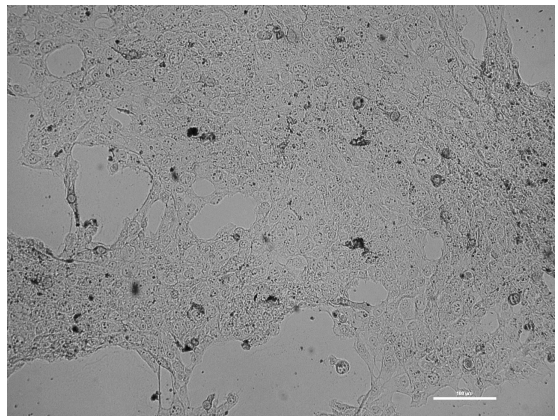

Figure 6.1: Image of the hFOB cells at day 0, scale bar equal to $100\mu m$.

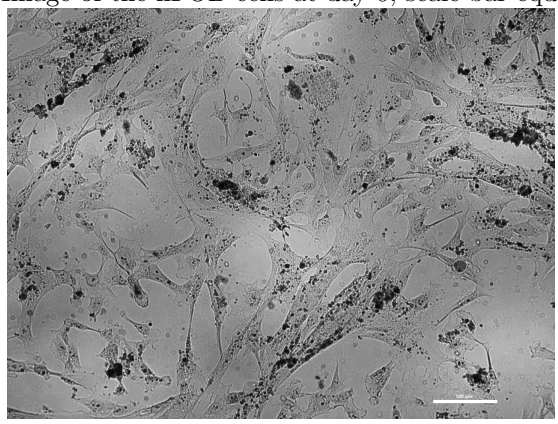

Figure 6.2: Image of the hFOB cells atfer 15 days of maturation, scale bar equal to $100\mu m$.

Cells grown at a temperature of 33.5°C exhibit rapid cell division (doubling in 36 hours), whereas little cell division occurs at a temperature of 39.5°C (doubling in 96 hours). These cells have the ability to differentiate into mature osteoblasts expressing the normal osteoblast phenotype. A 39.5°C cell division is slowed, differentiation increases, and a more mature osteoblast phenotype is produced. A panel of both consolidated and novel biophysics approaches are applied to assess osteoblast mechanical and morphological features, and results are correlated to cell maturation. The set

of exploited tools include staining, labelling and quantitative PCR (qPCR) techniques to assess cells functional levels, nanoindentation approach to shed light on cellular elastic response, and quantitative phase imaging strategies to obtain quantitative and qualitative cell morphology information. Nanoindentation experiments were performed at day 0, Fig. 6.1, meaning that cells were still at 33.5°C, and then, after increasing temperature up to 39.5°C, experiments were performed after 5 days, 11 days and 15 days, Fig. 6.2 . In order to study this global phenomenon that affects cell phenotype at different levels, a simpler schematization of the cell is sufficient. Therefore the DFIT procedure is applied for the data analysis. Nanoindentation experiments were performed using Piuma Chiaro. The probe used in this work was a glass sphere with a radius of $10.5\mu m$ and a stiffness of $.116N/m$, suitable for measuring objects in the range of $0.5 - 100kPa$. For each experimental condition $100 - 150$ curves were acquired over at least 3 different repeats. Results are shown in Fig. 6.3.

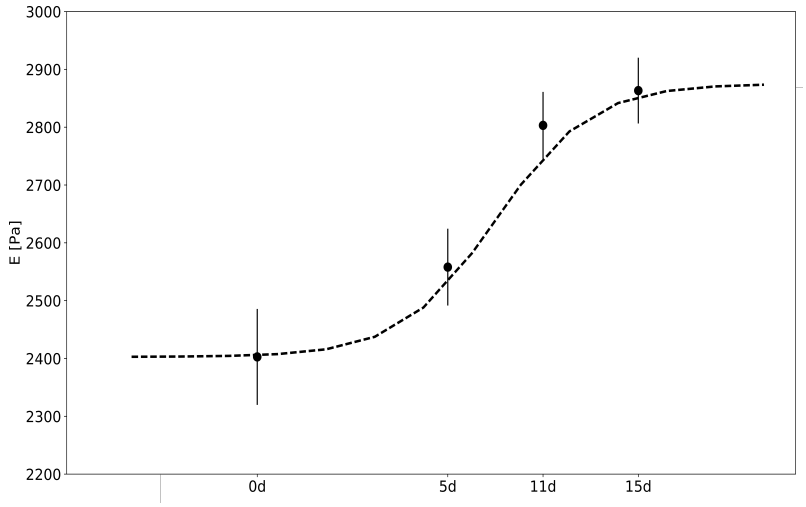

Figure 6.3: The elastic modulus during osteoblast maturation changes significatively.

The stiffness appears to increase in time while maturation occurs. The same cells were tested also through holographic microscopy, in order to characterize osteoblastic maturation also from a morphometric point of view.

In figure 6.4 a significativity map is represented. One way Anova statistical test is performed pairwise in order to estimate if there are statistical significative differences among the conditions.

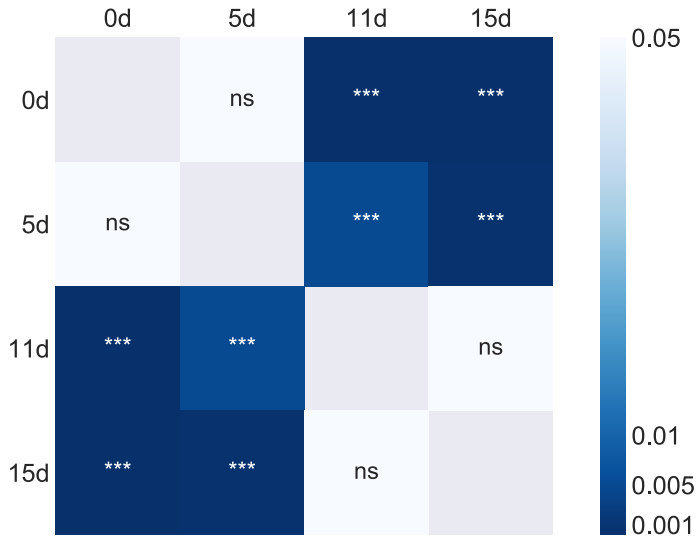

Figure 6.4: Significativity map: statistical significance is computed pairwise using one way Anova statistical test.

The progression of osteoblast maturation is usually accompanied by changes in the expression of several bone related genes. This was assessed by quantitative Real Time PCR experiments and the results are summarised in the histogram of Fig. 6.5. Among the markers tested in the experiments Osteocalcin (BGLAP/OC), Osteopontin (SSP1/OP), integrin bindig sialoprotein (IBSP) and the epigenetic regulator (KDM6A) were included. According to the generally accepted model, the first three markers are up regulated in the second stage of osteoblast maturation, when genes of connected to proliferation are down regulated and those correlated with ECM maturation

are activated [56]. Indeed, independent of the considered time point , all the cells grown at 39.5°C show an increased expression of these markers than the cells grown at 33.5°C, thus confirming that a maturation process is occurring in our samples. The fourth gene, KDM6A a chromatin regulator encoding a specific histone lysin demetilase has been previously connected with osteogenesis in MSC cells [27]; its up regulation in non proliferating hFOB cells indicate an involvement of this protein also in hFOB maturation. In order

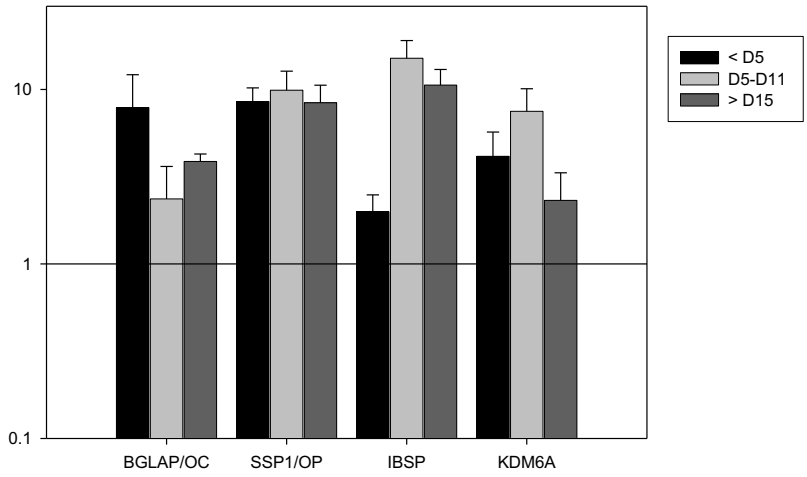

Figure 6.5: Expression of specific osteogenic markers along hFOB maturation. The results were obtained from three different experiments in which each gene was assessed in triplicate.

to quantitatively characterize osteoblasts shape changes during their maturation steps DH technology has been exploited, which allowed the evaluation of various morphological parameters such as cell area, perimeter, roughness, eccentricity, irregularity, thickness, and volume, in a label-free mode. Trends of morphometric and elastic features during time steps have been correlated pairwise, considering for each dataset both the values and their standard deviations, using Pearson correlation index contained in Python Pandas library (https://pandas.pydata.org). A correlation matrix was produced of

the mostly correlated features Fig. 6.6.

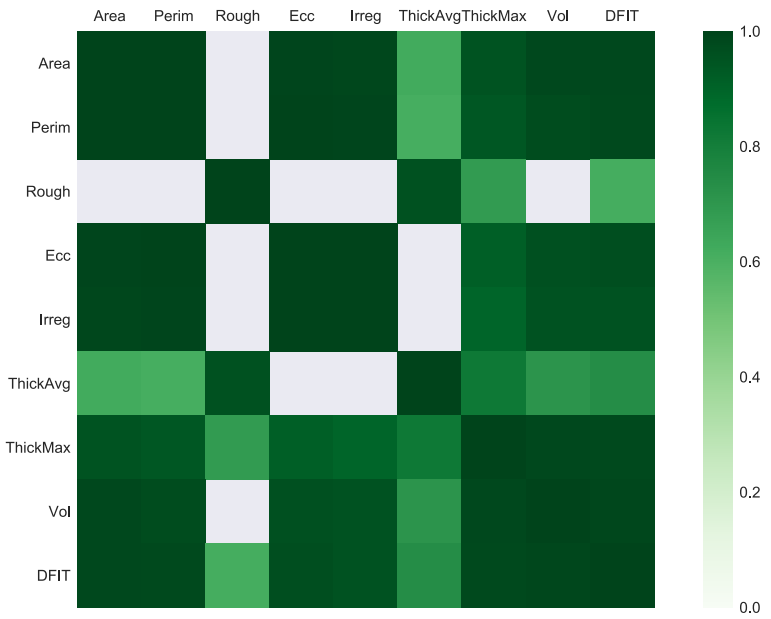

Figure 6.6: Matrix correlation of morphological parameters and elasticity.

In the correlation matrix are shown just values of correlation higher than 0.6. Stiffness in time results to be highly correlated with several morphometric parameters. In particular, the evolution of osteoblasts stiffness, acquired over time in proliferation and differentiation modes (dependent on colture temperature), results to be highly correlated with modification in osteoblasts occupancy area, their perimeter, their eccentricity factor, their surface irregularity, their maximum thickness and their volume.

6.3 FaO cells

The liver is not a primary fat storage depot and the steady state concentration of hepatic triglycerides (TGs) is rather low under physiological conditions. Excess TG accumulation in hepatocytes results in nonalcoholic fatty liver disease (NAFLD), the metabolic liver disease which attracts ever more attention in Western countries for its increasing prevalence as consequence of overnutrition. NAFLD encompasses a spectrum of liver abnormalities ranging from the simple steatosis, to nonalcoholic steatohepatitis (NASH), to cirrhosis and hepatocarcinoma [9], [41]. Steatosis in NAFLD typically results from an imbalance in lipid metabolism pathways. The excess TGs resulting from either excess fatty acid (FA) intake or de novo lipogenesis are stored as cytosolic lipid droplets (LDs) [43], [60]. Number and morphometry of lipid droplets (LDs) define micro vs macrovesicular steatosis, influence the morphology and function of hepatocytes and possibly their stiffness. Indeed biomechanical properties of cells change in several diseases [16], and fat accumulation should influence the biomechanical properties of hepatocytes and trigger mechanosensitive processes. The progression of NAFLD in vivo is associated with an altered mechanical liver phenotype, in which the stiffness is strictly linked to organ dysfunction and used as a diagnostic marker [55]. A recent study indicated that LDs are stiffer than the surrounding cytoplasm so they may mechanically distort the intracellular environment [54]. Nevertheless, a connection between changes in biomechanical properties and altered physiological functions of the cell has not been yet identified, and do requires further investigations. We hypothesize that the mechanical properties of single hepatocytes could depend on the steatosis grade and LD features. A detailed biophysical single cell study of different steatotic models mimicking NAFLD progression in vitro was performed by Single Cell Force Spectroscopy (SCFS) [39] and high resolution Quantitative Phase Microscopy (QPM) [8] to verify whether and how the cell elasticity and the morphometric features of steatosis could be associated with different steatotic conditions. The link between qualitative/quantitative steatosis and biomechanical properties of single hepatocytes requires further investigations.

To mimic in vitro NAFLD progression rat hepatoma FaO cells were treated with:

- Fructose (Fru),
- Fatty acids (FA),
- Fructose+Fatty acids (Fru/FA)
- Fatty Acids+Tumor Necrosis Factor α (FA/TNFα).

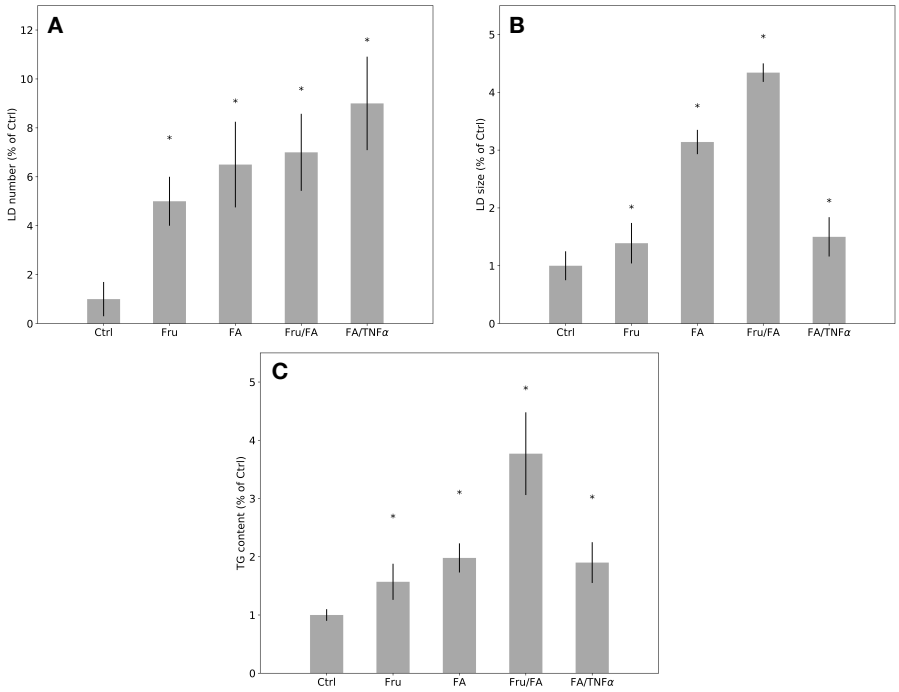

Figure 6.7: For FaO cells incubated in the absence (Ctrl) or in the presence of fructose (Fru), oleate/palmitate (FA), Fru/FA, FA/TNFα are shown: (A-B) average number of LDs/cell and size of LDs; (C) TG content expressed as percent TG content relative to controls, normalized for proteins determined with Bradford assay.

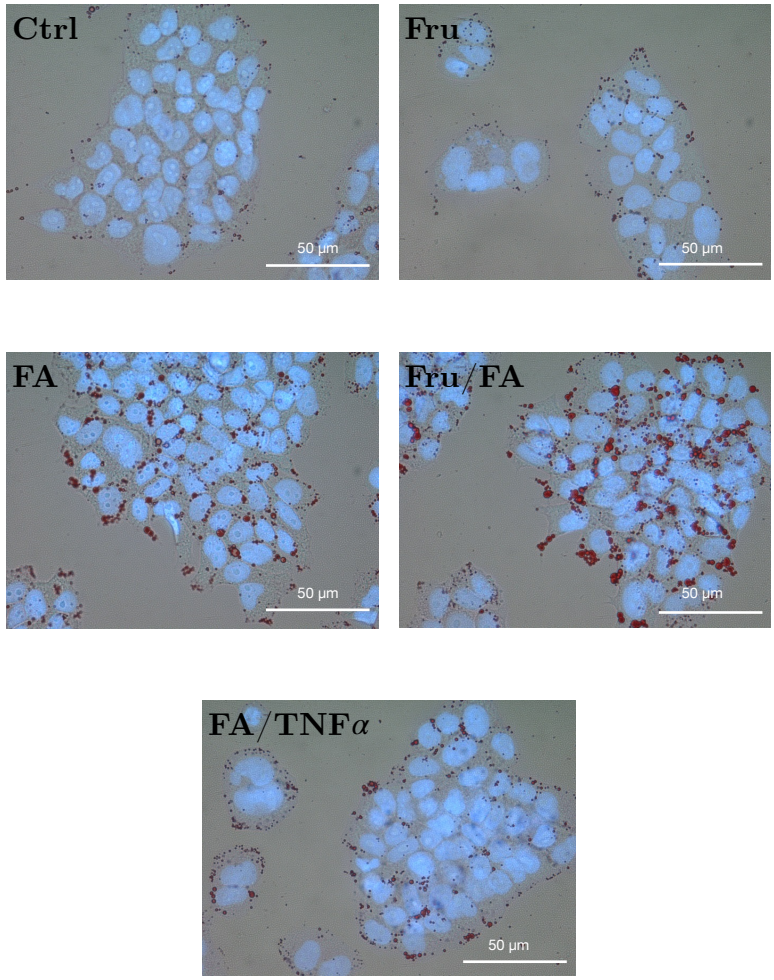

Figure 6.8: Neutral lipids were visualized by optical microscopy using the selective Oil-RedO (ORO) dye.

In this thesis it is reported only the section related to SCFS. Nanoindentation experiments were performed for all the treatments and force dis-

placement curves have been analysed using the DFIT method and the FIEL method. In the FIEL method the relative elasticity $E_{r,n}$ of a sample n was calculated with respect to the average of the control dataset, such as:

$$E_{r,n}^{FIEL} = \left(\frac{\langle w_{CTRL} \rangle}{w_n} \right)^{\frac{3}{2}}. \tag{6.1}$$

The result obtained with the DFIT procedure were computed relative to the mean value of the control condition to make it comparable with the results obtained with the FIEL method.

$$E_{r,n}^{HERTZ} = \frac{E_n}{\langle E_{CTRL} \rangle} \tag{6.2}$$

For each experimental condition $50-70$ curves were acquired over at least 3 different repeats and Table 6.9 collects the main results obtained with the FIEL method and the standard DFIT.

	FIEL			DFIT		
	Mean	SD	Shapiro	Mean	SD	Shapiro
Ctrl	1,026	0,181	0,971	1,367	0,459	0,903
Fru	1,214	0,277	0,919	1,731	0,725	0,890
Fru/FA	1,318	0,331	0,949	1,608	0,668	0,903
FA	1,223	0,330	0,885	1,975	1,186	0,747
FA/TNFα	1,184	0,350	0,853	1,536	0,780	0,802

Figure 6.9: Mean and standard deviation of the gaussian probability density function, fitted on the relative Young's modulus distribution, are presented for both the DFIT and the FIEL methods. The result of the Shapiro normality test on the distributions are shown in the third column for each method.

Data are fitted with Gaussian distributions because assumptions supporting the choice of a different distribution were not made. As depicted in 6.10, the relative elasticity E_r values obtained with the DFIT approach are more broadly distributed (SD 2 to 4 folds larger than the one obtained

with the FIEL method). Moreover, the FIEL distributions appear to resemble more closely a Gaussian distribution (Shapiro coefficient closer to 1) [53]. The FIEL analysis was purposely developed for this study, that required an unprecedented sensitivity and robustness in the quantification of the mechanical properties to resolve small changes with statistical relevance.

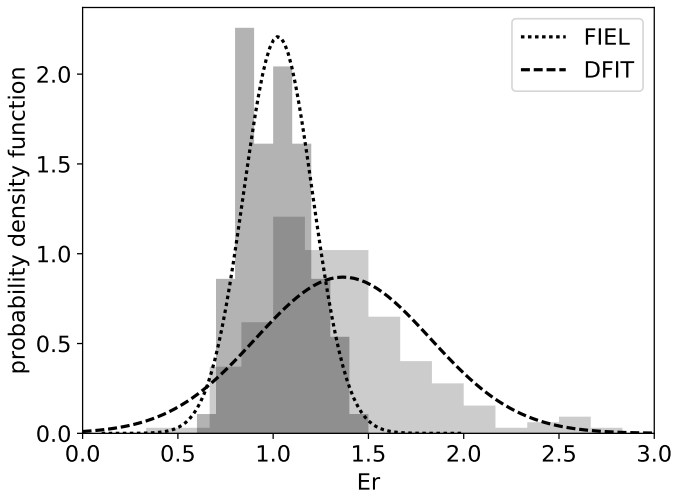

Figure 6.10: Probability density functions of both FIEL and DFIT methods.

The results of the FIEL approach (Fig. 6.11) showed that E_r significantly ($p \leq 0.05$) increased in cells exposed to either Fru or FAs as single agents (1.11 and 1.15 fold increase vs Ctrl, respectively;), and an even larger increase occurred in cells exposed to Fru/FA combination (1.17 fold increase vs Ctrl), although the increment with respect to FAs and Fru alone was not statistically significant. Conversely, the FA/TNFα combination increased the E_r (1.09 fold increase vs Ctrl) to a value similar to that observed for FAs alone.

In these models, combined Fru/FA resemble a condition of macrovesicular steatosis, whereas combined FA/TNFα lead to microvesicular steatosis. Hepatocyte biomechanics shows that cell stiffness is strongly influenced by fat accumulation. Indeed alterations of cell biomechanics might sustain the extent and speed of evolution of steatosis and liver stiffness in relation to the

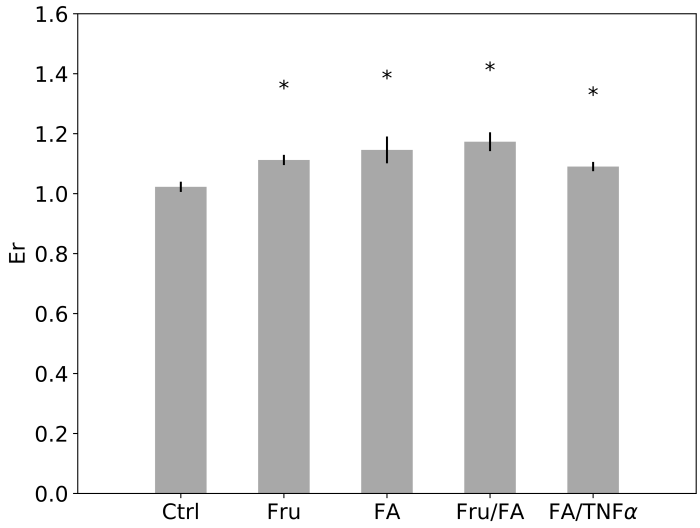

Figure 6.11: Relative Elasticity (E_r) of single cell respect to the control, obtained through the FIEL method. Symbols: Ctrl vs all treatments $p \leq 0.05$.

necro-inflammatory potentials and steatogenic inducer (e.g., dietary loads).

6.4 HEK cells

HEK 293 is a cell line, well known in literature, originally derived from human embryonic kidney cells grown in tissue culture, which has been used in this project to test also experimentally the efficiency of the elastography method. For this purpose HEK cells were treated with two different substances that are know interacting on specific components of the cell cytoskeleton. The cytoskeleton is a network of filamentous proteins providing structural support and integral tension [21], [25], [46]. Moreover it has been proved that it has a key role in mechanotransduction processes. The cytoskeleton is composed of three main elements: actin filaments, intermediate filaments and microtubules 6.12. Microtubules provide the basic organiza-

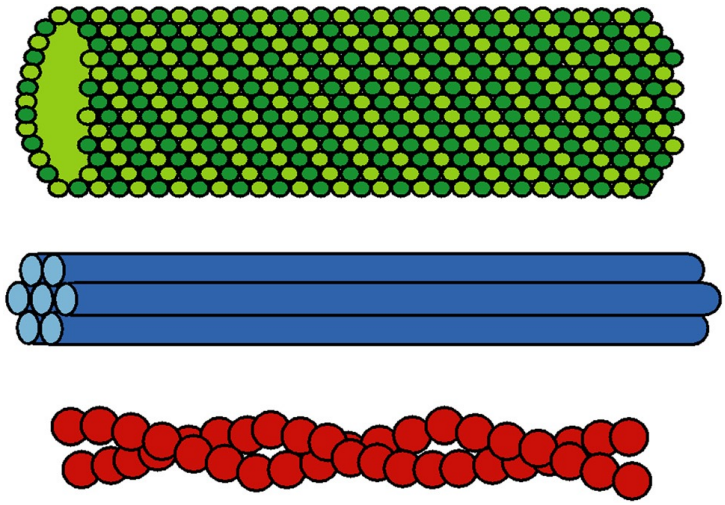

Figure 6.12: Three major protein filaments compose the cell cytoskeleton: microtubules (top), intermediate filaments (center), and actin filaments (bottom) [46].

tion of the cytoplasm, they grow dinamically (polymerization) and can resist compressive forces. Actin filaments are the main structural compomenents of the cytoskeleton and respond to external forces through deformation and rearrangement. They also make up the cell cortex, that is a specialized

layer on the inner face of the cell membrane, which is responsible for the modulation of the membrane properties and more generally of cell surface properties, Fig. 6.13. [12].

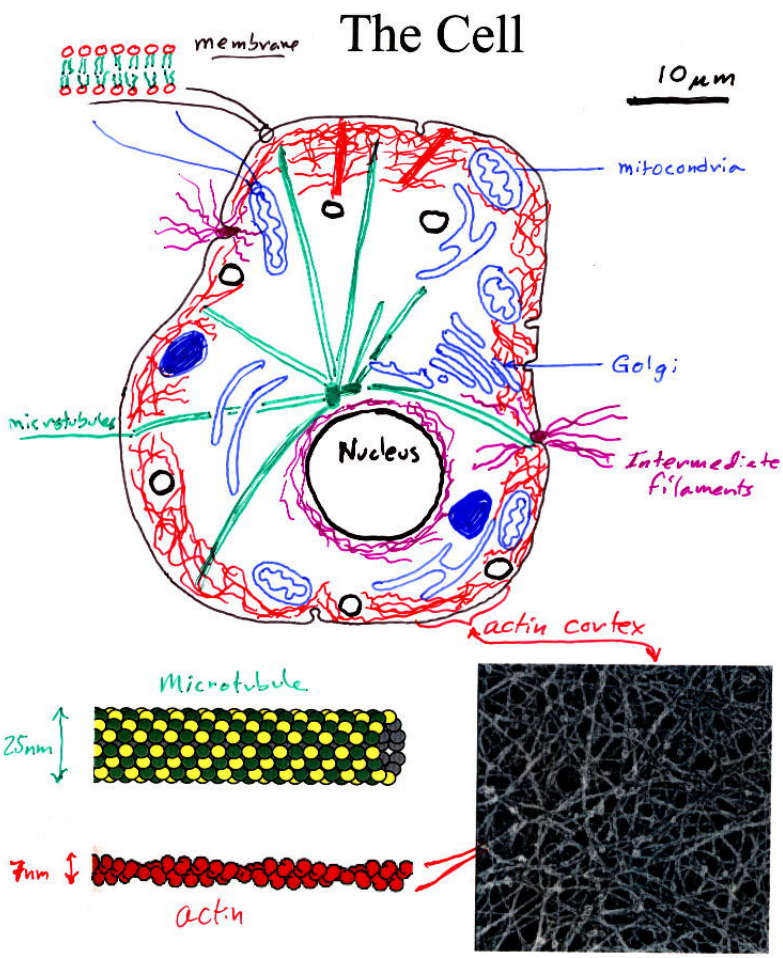

Figure 6.13: Cell schematization, [4]. Main cell structural components (microtubules and actin) are represented in the illustration. The actin cortex is located on the inner face of cell membrane.

HEK cells have been treated with Colchicine and Cytochalasine D, two molecules extensively used to selectively act on different cytoskeletal compartments, [57], [38], [39]. Colchicine is a toxic alkaloid that is know to inhibit microtubules polimerization by binding to tubulin. Cytochalasin D instead is a cell permeable fungal toxin that is used to disorganise actin filaments [14]. Cytochalasin D is dissolved in DMSO and used with a concentration of $10\mu M$.

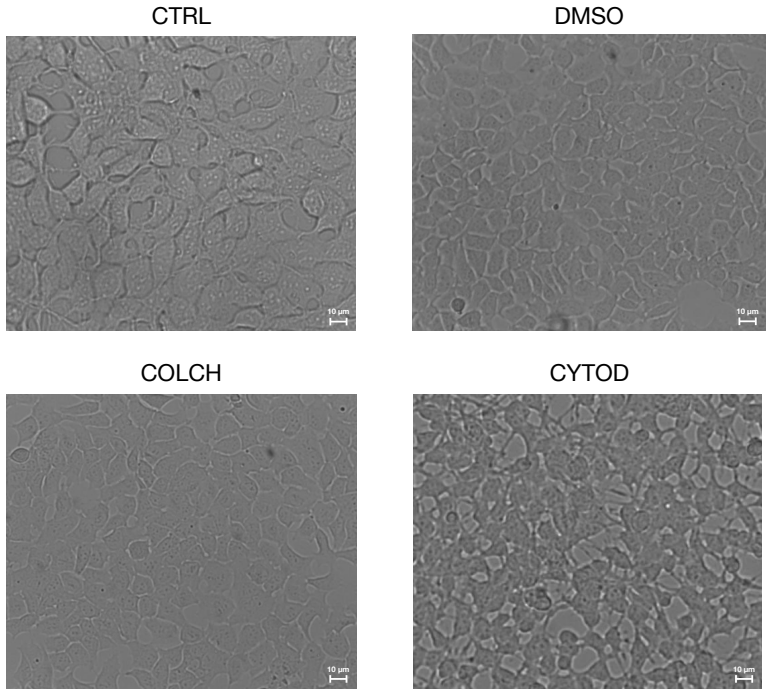

Figure 6.14: HEK cells images for all the conditions

Colchicine is dissolved in water and used with a concentration of $100\mu M$. Both treatments last 1 hour, while cells are incubated at 37°C. Because cytochalasin D is dissolved in DMSO, a toxic solvent, it should be ensured that changes in cell stiffness are due to cytochalasin and not to the solvent. In order to do that, another control experiment has been performed, placing

the equivalent amount of DMSO, necessary to dissolve the molecule, into the sample for 1 hour, during incubation. For each experimental condition $100-150$ curves were acquired over at least 3 different repeats. All the methods were compared for the analysis of these experiments. DFIT and FIEL, Fig. 6.15 and Fig. 6.16, show the same behaviour: stiffness is practically the same for all the conditions, except for the colchicine treatment that results in cell stiffening.

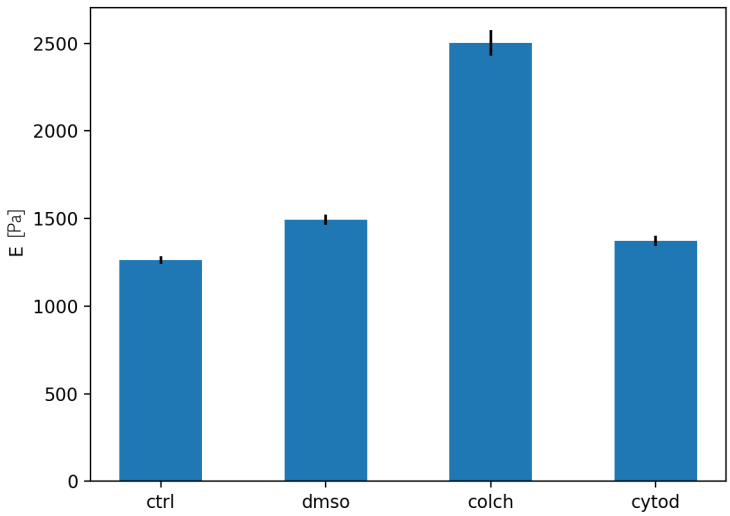

Figure 6.15: Elasticity (E) of single cell respect to the control, obtained through the Hertz method.

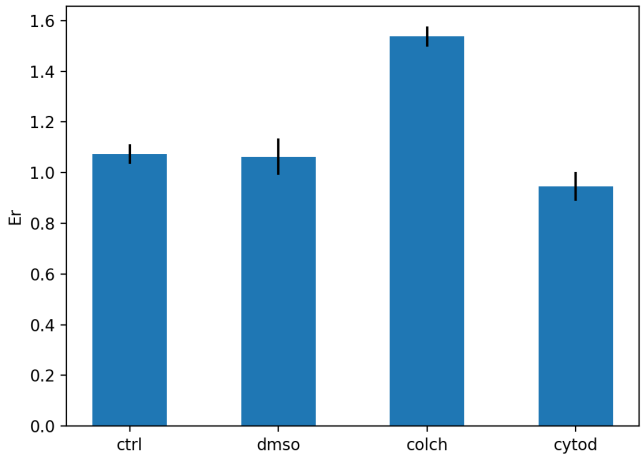

Figure 6.16: Relative Elasticity (E_r) of single cell respect to the control, obtained through the FIEL method.

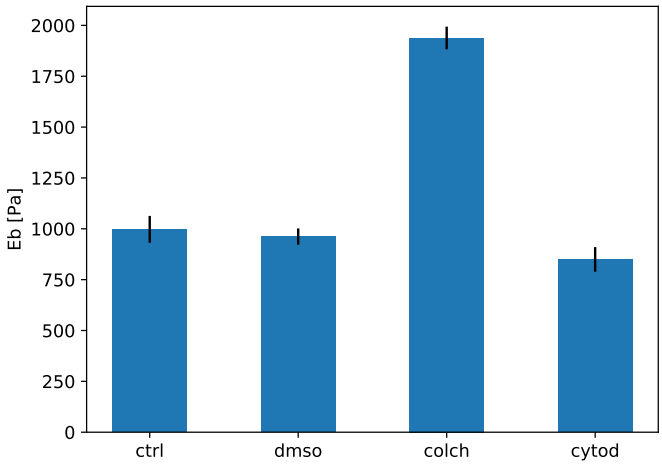

Figure 6.17: Elasticity (E_b) of the internal layer obtained through the Elastography method.

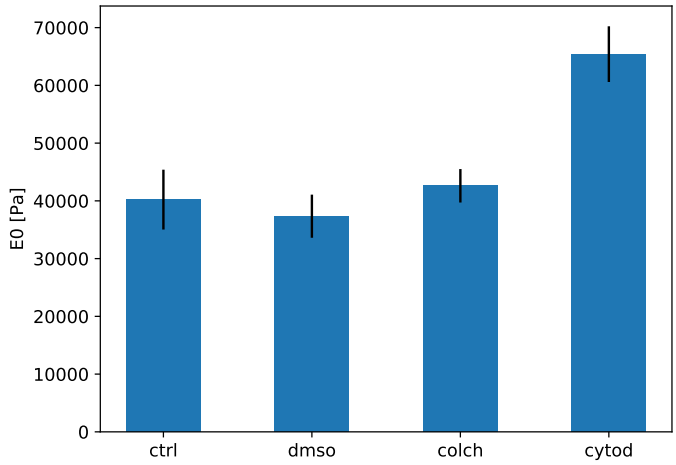

Figure 6.18: Elasticity (E_0) of the external layer obtained through the Elastography method.

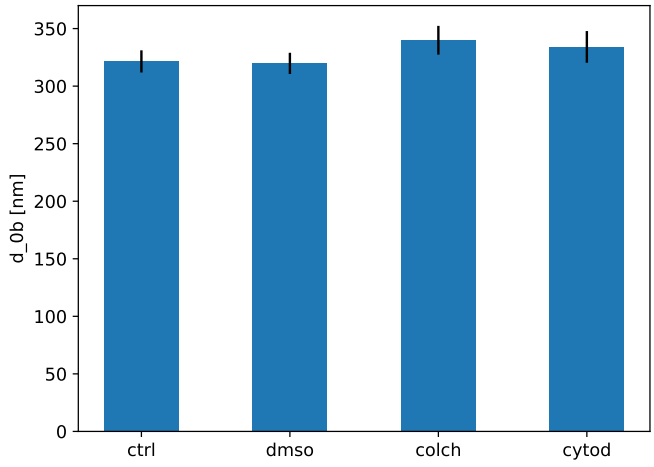

Figure 6.19: Thickness (d_{0b}) of the external layer obtained through the Elastography method.

Elastography, as shown in simulations, supports and increases the information gained with the standard methods. Indeed the internal layer stiffness E_b shows the same behaviour of the previous method, meaning that colchicine has a strong effect *inside* the cell, Fig. 6.20. This is consistent with microtubules polimerization inhibition induced by colchicine.

The Elastography method highlights changes in the external layer, otherwise undetectable by standard methods. Indeed cytochalasin D seems to induce a stiffening in the external layer, compatible with its effect on actin filaments of cell cortex, [6]. The external layer thickness seems to remain constant for all the conditions.

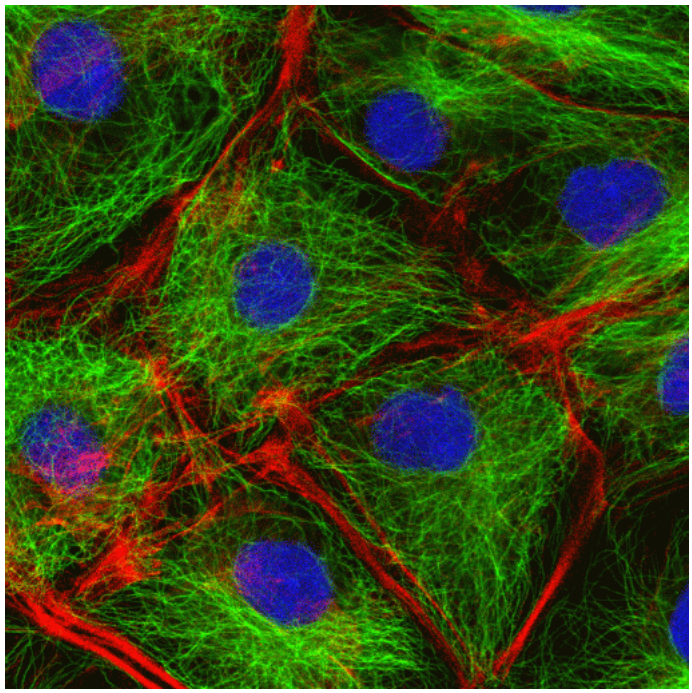

Figure 6.20: Cells stained with fluorescent labels to help visualise the cytoskeleton with microtubules (green), actin filaments (red), and the nucleus (blue). *British Society for Cell Biology*

6.5 A1 cells

A1 cells are a cell line from mice embryonic mesencephalon. A1 cells express neuronal markers and show a neuron-like behavior, thus can be a suitable model in some pharmacological studies in neurosciences and in researches concerning neurodegenerative diseases (in particular Alzheimer's), migraine and major depression [13], [22], [52]. Furthermore, a growing body of evidence suggests that mechanical properties of neurons plays a role in such pathologies and that changes in the biomechanics of the cells involved can induce or sustain the onset of cellular activities resulting in the symptoms themselves [62].

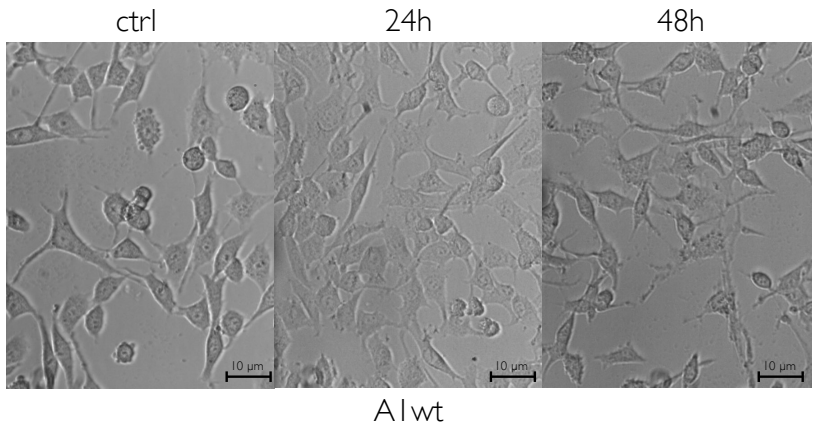

Figure 6.21: Images of the wild type a1 cells during the treatment with aβ.

The β-Amyloid fragment $(1-42)$ is involved in Alzheimer's disease, [34], and a1 cells treated with it show a degenerative process similar to the neuronal one typical of the disease. It is known that the prion is the stronger interactor of aβ $1-42$ in healthy neurons, even though no biochemical or signal pathway seems to be influenced by this interaction. Results obtained with single cell force spectroscopy, suggest that a1 cell populations express-

ing (wt) and not expressing (sh) the prion, treated and not treated with aβ1-42 show different elastic and biomechanical properties, Fig. 6.21 and Fig. 6.22. For each experimental condition $150 - 200$ curves were acquired over at least 3 different repeats.

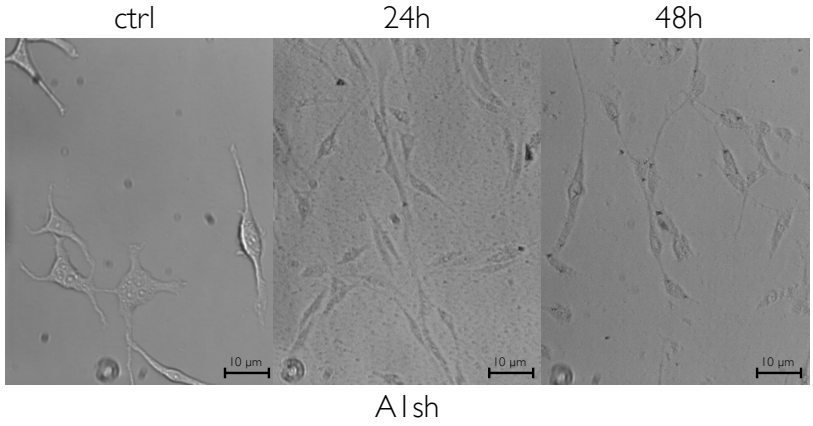

Figure 6.22: Images of the silenced for the prion a1 cells during the treatment with aβ.

Elastography is applied in this biological problem to highlight differences in time as a result of the aβ treatment.

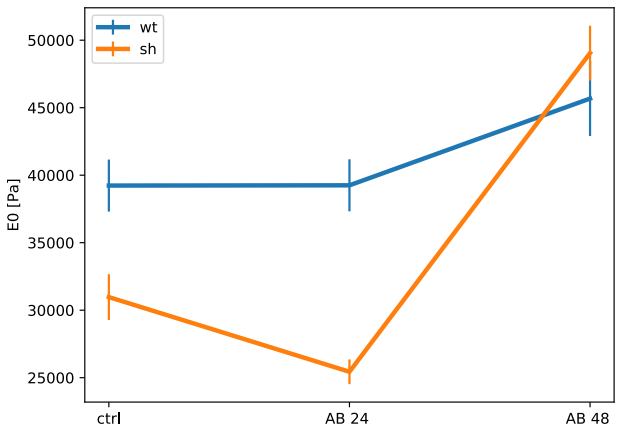

Figure 6.23: External layer stiffness.

Because of the shape found in the experimental Stiffness vs Indentation curve, the bilayer model approach was applied in the analysis. The parameters representing the bilayer stiffness are presented in Fig. 6.23, Fig. 6.24 and Fig. 6.25. The external layer stiffness increases in time in both the cell lines, while the internal one decreases as the thickness of the external layer. A biological explanation is currently being studied. The most likely explanations of this phenomenon are an alteration of the spatial organization of extracellular and intracellular membrane associated proteins together with the amyloids plaques newly formed and the composition of the lipid rafts and Ca^{2+} omeostasis [62], [50].

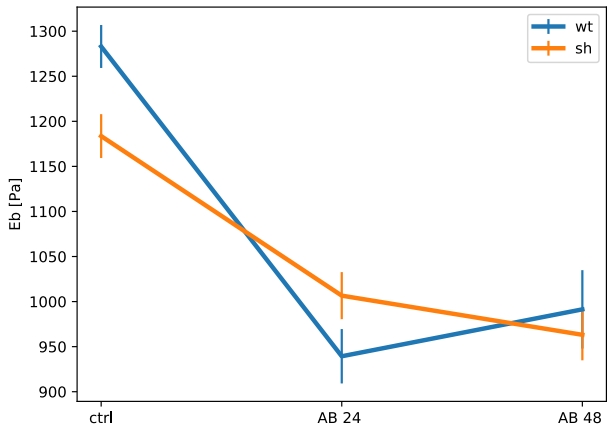

Figure 6.24: Internal layer stiffness.

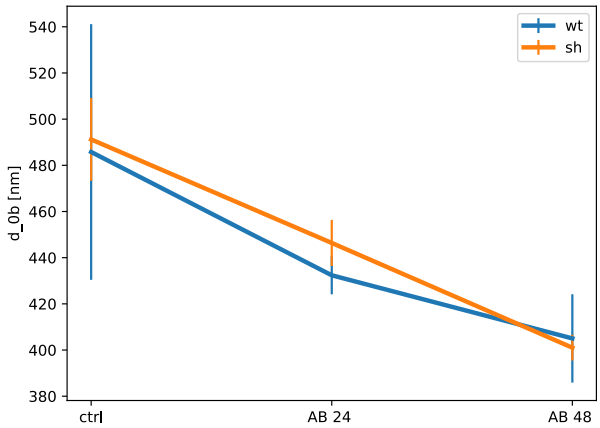

Figure 6.25: External layer thickness.

6.6 Piezo1

Piezo1 is a mechanosensitive ion channel involved in many mechanotransduction processes [15], [45]. However very little is known about its mechanism. In this project nanoindentation experiments were performed HEK cells with different Piezo1 patterns of expression. The Wild Type HEK cells (ctrl) display endogenous expression of Piezo1. The Piezo1 Knock In HEK cells (piezo1) show higher level of expression of this protein and, on the contrary, in the Knock Out Piezo1 HEK cells (ko) the expression of this channel is totally abolished.

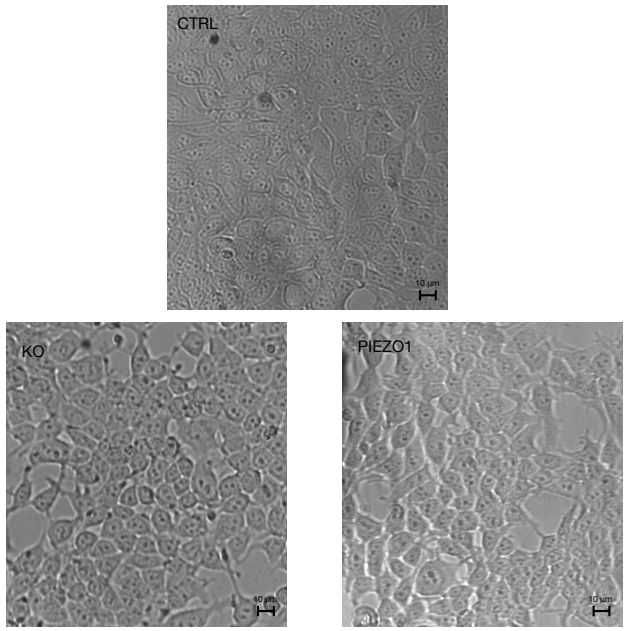

Figure 6.26: Picture of the three cell lines: the control cells (CTRL), the overexpressing piezo1 cells (PIEZO1) and the piezo1 knockout cells (KO).

The aim was the mechanical characterization of these cell lines, in order to infer if modification of the channel lead to changes in the biomechanics of the systems. For each experimental condition $200-250$ curves were acquired

over at least 3 different repeats. Elastography is used to perform the analysis also in this case.

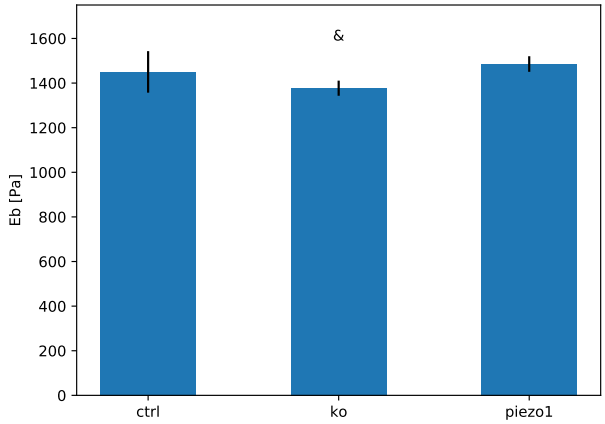

Figure 6.27: Internal layer stiffness.

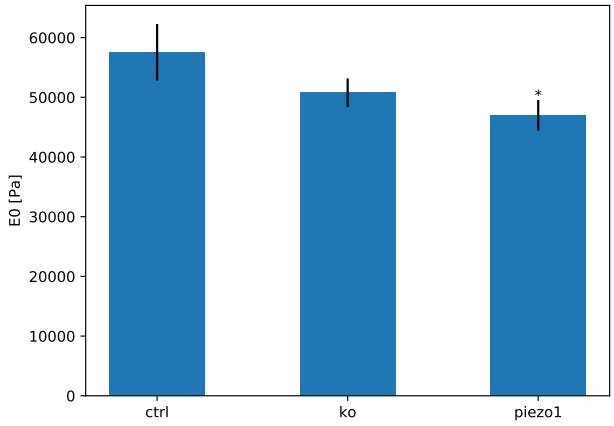

Figure 6.28: External layer stiffness.

Statistical significativity is indicated if at least $p \leq 0.05$. If it is computed respect to the control condition is marked with $'*'$, if respect to piezo1 with $'\&'$. The internal layer stiffness E_b is significatively reduced for the piezo1 knockout cells (ko) respect to the overexpressing cells (piezo1). The external layer stiffness instead seems to decrease for both the ko cells and piezo1, significatively respect to the control just for piezo1. The external layer thickness instead is higher for the piezo1 condition, significativity respect to the control and also to the ko.

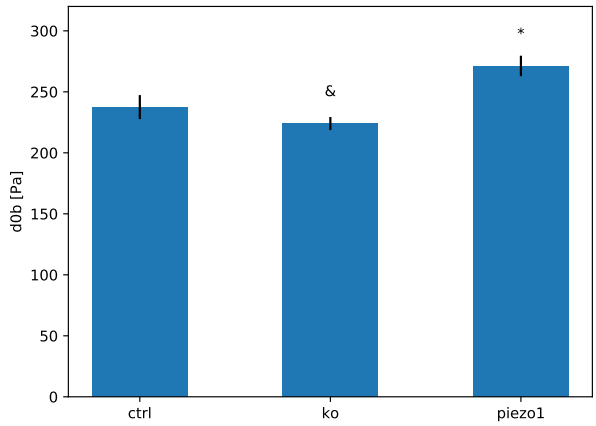

Figure 6.29: External layer thickness.

Chapter 7

Discussion

In this project three nanoindentation protocols have been studied and discussed in order to underline their main weaknesses, highlighting relevant dependences of the result on experimental conditions and anaytical steps. Different methods for data analysis have been proposed and tested in simulation and then applied in the experimental case. Several aspects of a nanoidentation experiments were considered, from the experimental protocol to the data analysis. Taking into account all the previous considerations, an optimal procedure was developed for unbiased nanoindentation experiments.

In simulation, all the three methods were tested on the bilayer model. The DFIT method, that finds an average absolute value for cell elasticity, identifies only the internal layer stiffness. The same considerations can be made regarding the FIEL method, that provides an average relative value of stiffness. The elastography, both in absolute and relative version, allows to derive the stiffness vs indentation curve of the bilayer. This was verified when the external layer is stiffer, but also when it is softer, adding noise to the force-indentation curve and in a specific range of the indentation depth.

The DFIT method has been used in the hFOB cells project in order to measure differences during cell maturation. If the method is used with all the caution it needs, above all in the tip-sample contact point determination, it can provide reasonably accurate results. Indeed the differences in time are significative and the stiffness trend correlates with the morphological changes. However, reliable results - in terms of measuring differences - are better noticed if the relative method FIEL is applied. In the FaO

cells project, advantages of preferring relative methods to absolute ones are demonstrated. Data distributions are tighter and more Gaussian for the FIEL method with respect to the DFIT one. This grants that small significant changes can be easier resolved from the relative method. These approaches can be used when one average parameter is considered sufficient to describe the whole cell mechanical properties. If a label-free biomarker, robust and reliable, is needed to address changes or differences of the biological system of interest, then DFIT and FIEL are a suitable choice. On the other hand, if the biological problem requires a deeper characterization of the changes that are affecting the system, the Elastography is more suitable as it provides a result with a greater degree of detail, starting from the same raw data that the standard methods use.

The Elastography method provides in the general case a Stiffness vs Indentation depth curve that can reveal far more information about cell mechanics. If the experimental curve matches the bilayer stiffness curve, then the parameters describing the curve can be computed with great accuracy. In this case, the standard methods DFIT and FIEL, can identify just the internal layer. This has been proved in simulation, but also as a experimental result in the HEK cells project. Indeed, the same result obtained for the internal layer stiffness with Elastography is obtained using the FIEL and DFIT methods, meaning that the information achieved with the standard methods is still embedded in the Elastrography. Therefore, Elastography truly allows a deeper insight into cell mechanical properties: in the bilayer case the external layer can be characterized in terms of stiffness and thickness.

These satisfactory results led to deploy Elastography in solving relevant problems. This happened for the A1 cells project where alterations induced by aβ have been appreciated in terms of external and internal layer stiffness and external layer thickness. The same approach has been applied to the Piezo1 project, in which the correlation between the ion channels expression and the biomechanics of the system has been addressed. Infact, the effects of a different expression of the channel protein occur in a different behaviour of the parameters obtained with Elastography, especially the elasticity of the external layer and its thickness, which shown significative differences in the three cell lines.

In conclusion Elastography proves itself to be a valuable method for the evaluation of fine changes in cellular biomechanics, due to alterations of structural components of the cell. Specifically it is a useful tool to discrimi-

nate changes regarding cytoskeletal components, such as microtubules fuses and the actin cortex, as it has been proved in the project concerning the HEK cells.

Chapter 8

Conclusion

This chapter summarizes the contribution of the thesis and discusses avenues for future research.

8.1 Summary of contribution

Measuring absolute elasticity through nanoindentation experiments is tricky and obtaining reliabe results is not trivial. It requires an accurate design of the experiments, as well as data analysis procedures. Relative approaches are more efficient and robust in this sense, allowing to better evaluate differences in cell mechanics. The elastography allows a deeper insight into cell structure, going beyond the average value found by the standard methods. The outcome is a Stiffness vs Indentation curve, without any a priori assumptions on the elasticity model of the sample. If the sample can be represented as a bilayer, then Elastography allows to identify the characteristic parameters. This has been proved in simulation and in experimental environment. Indeed, in the project involving HEK cells treated with colchicine and cytochalasine, Elastography verified the effects of the two molecules each on a different layer. In the project regarding hFOB cells, the DFIT analysis has highlighted biomechanical changes during maturation and the correlation between cell stiffness and morphology. In the project with FaO cells, epatoma cells have been treated to mimic in vitro nonalcoholic fatty liver deasease. Significative differences in the treatments have been identified using the FIEL method and the correlation between hepatocytes biomechanics and fat accumulation has been addressed. The Elastography has been used

to analyse nanoindentation experiments on A1 cells treated with aβ, one of the protein involved in Alzheimer's disease. This allowed to detect biomechanical changes as a function of time, after the cells have been treated. Then, Elastography has been used to verify if modification in the expression of the mechanosensitive ion channel Piezo1 leads to changes in the biomechanics of the cell. Therefore, the goal of developing a method able to find correlations between the biomechanics of the system and its mechanobiology has been achieved.

8.2 Directions for future work

From a technical point of view, the main goal of the next future is to release an open source software for an automatic analysis of nanoindentation experiment measurements. This consists in extending the software already developed for generic nanoindentation curves, introducing an interface allowing to choose between methods and set the analysis parameters. The idea is that the software should perform automatically all the analysis, even the selection between curves that can be analysed and curves to be discarded. This is already ongoing via neural networks. Moreover, Elastography can be applied to other relevant biological problems, to detect changes with an higher grade of information. From a theorical point of view, it could be interesting extending the bilayer model. Indeed, it happens that stiffness vs indentation curve, computed in the firts step of the Elastography, doesn't match the bilayer model. In this case, usually the curves are bath-tube shaped or showing a softer layer. A reasonable explanation of this behaviour could be found in the interaction with the stiffer substrate or with the cell nucleus, during the indentation. Thus, a third layer of different elasticity could be included in the model and the Elastography approaches could be adapted to reveal also its characteristics.

Appendix A

Publications

This research activity has led to several publications in international journals and conferences. These are summarized below.

International Journals

1. F. Baldini* A. Bartolozzi*, A. Voci, P. Portincasa, M. Vassalli e L. Vergani, Biomechanics of cultured hepatic cells during different steatogenic hits, Journal of Hepatology 2018, submitted.

2. Bartolozzi A., Basso M., Vassalli M., Single celle elastography from nanoindentation experiments (writing)

3. Bartolozzi A., Basso M., Gavazzo P., Sbrana F., Petecchia L., Vassalli M., Viti F. Development of biophysical label-free biomarkers in osteogenic development (writing)

International Conferences and Workshops

1. Soloperto A., Bartolozzi A., Palazzolo G., Basso M., Contestabile, A., Vassalli M., Difato F. Expression and biophysical characterization of bacterial mechano sensitive ion channel of large conductance into mammalian cells. 60th Biophysical Society Annual Meeting, February 27-March 2, 2016

2. Bartolozzi A., Soloperto A., Palazzolo G., Basso M., Difato F., Vassalli M. Real time identification of cell mechanical properties. 61st

Biophysical Society Annual Meeting, February 11-15 2017.

National Conferences

1. Bartolozzi A., Soloperto A., Palazzolo G., Basso M., Difato F., Vassalli M. Real time identification of cell mechanical properties. XXIII National Congress SIBPA, September 18-22 2016

2. Bartolozzi A., Basso M. , Difato F., De Stefano S., Vassalli M. Identification of robust biomarker from nano indentation experiments, Nanoengineering for Mechanobiology, March, 26-29 2017, National Research Council (CNR) and Swiss Federal Institute of Technology (ETH)

3. A robust approach from nanoindentation experiments, XXIV National Congress SIBPA, September, 10-13 2018, SocietàÂ Italiana di Biofisica Pura e Applicata SIBPA

Bibliography

[1] [Online]. Available: http://events.embo.org/17-cell-mechanics/

[2] [Online]. Available: http://optics11.com

[3] [Online]. Available: https://docs.scipy.org/doc/scipy/reference/generated/scipy.stats.f_oneway.html

[4] [Online]. Available: http://bio2.phys.kyushu-u.ac.jp/research_eng.html

[5] D. Anselmetti, *Single cell analysis: technologies and applications*. John Wiley & Sons, 2009.

[6] Y. A. Ayala, B. Pontes, B. Hissa, A. C. M. Monteiro, M. Farina, V. Moura-Neto, N. B. Viana, and H. M. Nussenzveig, "Effects of cytoskeletal drugs on actin cortex elasticity," *Experimental cell research*, vol. 351, no. 2, pp. 173–181, 2017.

[7] H. Babahosseini, "Single cell biomechanical phenotyping using microfluidics and nanotechnology," Ph.D. dissertation, Virginia Tech, 2016.

[8] E. Barone-Nugent, A. Barty, and K. Nugent, "Quantitative phase-amplitude microscopy i: optical microscopy," *Journal of microscopy*, vol. 206, no. 3, pp. 194–203, 2002.

[9] E. M. Brunt, V. W.-S. Wong, V. Nobili, C. P. Day, S. Sookoian, J. J. Maher, E. Bugianesi, C. B. Sirlin, B. A. Neuschwander-Tetri, and M. E. Rinella, "Nonalcoholic fatty liver disease," *Nature reviews Disease primers*, vol. 1, p. 15080, 2015.

[10] G. Caluori, J. Pribyl, M. Pesl, J. Oliver-De La Cruz, G. Nardone, P. Skladal, and G. Forte, "Advanced and rationalized atomic force microscopy analysis unveils specific properties of controlled cell mechanics," *Frontiers in Physiology*, vol. 9, p. 1121, 2018. [Online]. Available: https://www.frontiersin.org/article/10.3389/fphys.2018.01121

[11] J. Chen, "Nanobiomechanics of living cells: a review," *Interface focus*, vol. 4, no. 2, p. 20130055, 2014.

[12] P. Chugh and E. K. Paluch, "The actin cortex at a glance," *J Cell Sci*, vol. 131, no. 14, p. jcs186254, 2018.

[13] G. L. Colucci-D'Amato, A. Tino, R. Pernas-Alonso, U. di Porzio *et al.*, "Neuronal and glial properties coexist in a novel mouse cns immortalized cell line," *Experimental cell research*, vol. 252, no. 2, pp. 383–391, 1999.

[14] J. A. Cooper, "Effects of cytochalasin and phalloidin on actin." *The Journal of cell biology*, vol. 105, no. 4, pp. 1473–1478, 1987.

[15] B. Coste, J. Mathur, M. Schmidt, T. J. Earley, S. Ranade, M. J. Petrus, A. E. Dubin, and A. Patapoutian, "Piezo1 and piezo2 are essential components of distinct mechanically activated cation channels," *Science*, vol. 330, no. 6000, pp. 55–60, 2010.

[16] D. Di Carlo, "A mechanical biomarker of cell state in medicine," *Journal of laboratory automation*, vol. 17, no. 1, pp. 32–42, 2012.

[17] A. Elosegui-Artola, E. Bazellières, M. D. Allen, I. Andreu, R. Oria, R. Sunyer, J. J. Gomm, J. F. Marshall, J. L. Jones, X. Trepat, and P. Roca-Cusachs, "Rigidity sensing and adaptation through regulation of integrin types," *Nature Materials*, vol. 13, pp. 631 EP –, 05 2014. [Online]. Available: http://dx.doi.org/10.1038/nmat3960

[18] A. Emad, W. F. Heinz, M. D. Antonik, N. P. D'Costa, S. Nageswaran, C.-A. Schoenenberger, J. H. Hoh *et al.*, "Relative microelastic mapping of living cells by atomic force microscopy," *Biophysical journal*, vol. 74, no. 3, pp. 1564–1578, 1998.

[19] A. J. Engler, S. Sen, H. L. Sweeney, and D. E. Discher, "Matrix elasticity directs stem cell lineage specification," *Cell*, vol. 126, no. 4, pp. 677–689, 2006.

[20] G. Fenteany, P. A. Janmey, and T. P. Stossel, "Signaling pathways and cell mechanics involved in wound closure by epithelial cell sheets," *Current biology*, vol. 10, no. 14, pp. 831–838, 2000.

[21] D. A. Fletcher and R. D. Mullins, "Cell mechanics and the cytoskeleton," *Nature*, vol. 463, no. 7280, p. 485, 2010.

[22] M. T. Gentile, Y. Nawa, G. Lunardi, T. Florio, H. Matsui, and L. Colucci-D'Amato, "Tryptophan hydroxylase 2 (tph 2) in a neuronal cell line: modulation by cell differentiation and nrsf/rest activity," *Journal of neurochemistry*, vol. 123, no. 6, pp. 963–970, 2012.

[23] G. Gruca, S. De Man, M. Slaman, J. Rector, and D. Iannuzzi, "Ferrule-top micromachined devices: design, fabrication, performance," *Measurement Science and Technology*, vol. 21, no. 9, p. 094033, 2010.

[24] N. Guz, M. Dokukin, V. Kalaparthi, and I. Sokolov, "If cell mechanics can be described by elastic modulus: study of different models and probes used in indentation experiments," *Biophysical journal*, vol. 107, no. 3, pp. 564–575, 2014.

[25] K. Haase and A. E. Pelling, "Investigating cell mechanics with atomic force microscopy," *Journal of The Royal Society Interface*, vol. 12, no. 104, p. 20140970, 2015.

[26] S. M. A. Haghparast, T. Kihara, and J. Miyake, "Distinct mechanical behavior of hek293 cells in adherent and suspended states," *PeerJ*, vol. 3, p. e1131, 2015.

[27] S. Hemming, D. Cakouros, S. Isenmann, L. Cooper, D. Menicanin, A. Zannettino, and S. Gronthos, "Ezh2 and kdm6a act as an epigenetic switch to regulate mesenchymal stem cell lineage specification," *Stem cells*, vol. 32, no. 3, pp. 802–815, 2014.

[28] H. Hertz, D. E. Jones, and G. A. Schott, *Miscellaneous papers*. Macmillan and Company, 1896.

[29] E. Hodzic, "Single-cell analysis: Advances and future perspectives," *Bosnian journal of basic medical sciences*, vol. 16, no. 4, p. 313, 2016.

[30] H. Huang, R. D. Kamm, and R. T. Lee, "Cell mechanics and mechanotransduction: pathways, probes, and physiology," *American Journal of Physiology-Cell Physiology*, vol. 287, no. 1, pp. C1–C11, 2004.

[31] P. A. Janmey, "The cytoskeleton and cell signaling: component localization and mechanical coupling," *Physiological reviews*, vol. 78, no. 3, pp. 763–781, 1998.

[32] K. A. Jansen, D. M. Donato, H. E. Balcioglu, T. Schmidt, E. H. Danen, and G. H. Koenderink, "A guide to mechanobiology: where biology and physics meet," *Biochimica et Biophysica Acta (BBA)-Molecular Cell Research*, vol. 1853, no. 11, pp. 3043–3052, 2015.

[33] K. L. Johnson, K. Kendall, and A. Roberts, "Surface energy and the contact of elastic solids," *Proc. R. Soc. Lond. A*, vol. 324, no. 1558, pp. 301–313, 1971.

[34] K. A. Kellett and N. M. Hooper, "Prion protein and alzheimer disease," *Prion*, vol. 3, no. 4, pp. 190–194, 2009.

[35] J. K.L., *Contact Mechanics*. Cambridge University Press, 1985.

[36] G. Y. Lee and C. T. Lim, "Biomechanics approaches to studying human diseases," *Trends in biotechnology*, vol. 25, no. 3, pp. 111–118, 2007.

[37] M. Li, D. Dang, L. Liu, N. Xi, and Y. Wang, "Atomic force microscopy in characterizing cell mechanics for biomedical applications: a review," *IEEE transactions on nanobioscience*, vol. 16, no. 6, pp. 523–540, 2017.

[38] L. Liu, Z. Wang, W. Zhang, X. Zhu, L. Li, and Z. Weng, "Analysis of colchicine-induced effects on hepatoma and hepatocyte cells by atomic force microscopy," *Journal of nanoscience and nanotechnology*, vol. 18, no. 6, pp. 4248–4254, 2018.

[39] A. Mescola, S. Vella, M. Scotto, P. Gavazzo, C. Canale, A. Diaspro, A. Pagano, and M. Vassalli, "Probing cytoskeleton organisation of neuroblastoma cells with single-cell force spectroscopy," *Journal of Molecular Recognition*, vol. 25, no. 5, pp. 270–277, 2012.

[40] E. Moeendarbary and A. R. Harris, "Cell mechanics: principles, practices, and prospects," *Wiley Interdisciplinary Reviews: Systems Biology and Medicine*, vol. 6, no. 5, pp. 371–388, 2014.

[41] T. Nagaya, N. Tanaka, M. Komatsu, T. Ichijo, K. Sano, A. Horiuchi, S. Joshita, T. Umemura, A. Matsumoto, K. Yoshizawa *et al.*, "Development from simple steatosis to liver cirrhosis and hepatocellular carcinoma: a 27-year follow-up case," *Clinical journal of gastroenterology*, vol. 1, no. 3, pp. 116–121, 2008.

[42] A. W. Orr, B. P. Helmke, B. R. Blackman, and M. A. Schwartz, "Mechanisms of mechanotransduction," *Developmental cell*, vol. 10, no. 1, pp. 11–20, 2006.

[43] C. Postic and J. Girard, "Contribution of de novo fatty acid synthesis to hepatic steatosis and insulin resistance: lessons from genetically engineered mice," *The Journal of clinical investigation*, vol. 118, no. 3, pp. 829–838, 2008.

[44] L. Puricelli, M. Galluzzi, C. Schulte, A. Podestà, and P. Milani, "Nanomechanical and topographical imaging of living cells by atomic force microscopy with colloidal probes," *Review of Scientific Instruments*, vol. 86, no. 3, p. 033705, 2015.

[45] S. S. Ranade, R. Syeda, and A. Patapoutian, "Mechanically activated ion channels," *Neuron*, vol. 87, no. 6, pp. 1162–1179, 2015.

[46] M. L. Rodriguez, P. J. McGarry, and N. J. Sniadecki, "Review on cell mechanics: experimental and modeling approaches," *Applied Mechanics Reviews*, vol. 65, no. 6, p. 060801, 2013.

[47] A. Sameur, H. Yin, D. Duhamel, and V. Vilke, "A simple model for elastic and viscoelastic punch indentation problems with experimental validation," *arXiv preprint arXiv:0802.0241*, 2008.

[48] R. W. Schafer, "What is a savitzky-golay filter?[lecture notes]," *IEEE Signal processing magazine*, vol. 28, no. 4, pp. 111–117, 2011.

[49] H. Schillers, C. Rianna, J. Schäpe, T. Luque, H. Doschke, M. Wälte, J. J. Uriarte, N. Campillo, G. P. Michanetzis, J. Bobrowska *et al.*, "Standardized

nanomechanical atomic force microscopy procedure (snap) for measuring soft and biological samples," *Scientific reports*, vol. 7, no. 1, p. 5117, 2017.

[50] M. Schmitz, K. Wulf, S. C. Signore, W. J. Schulz-Schaeffer, P. Kermer, M. Bähr, F. S. Wouters, S. Zafar, and I. Zerr, "Impact of the cellular prion protein on amyloid-β and 3po-tau processing," *Journal of Alzheimer's Disease*, vol. 38, no. 3, pp. 551–565, 2014.

[51] U. S. Schwarz, "Mechanobiology by the numbers: a close relationship between biology and physics," *NATURE REVIEWS— MOLECULAR CELL BIOLOGY*, vol. 18, p. 711, 2017.

[52] V. Severino, A. Farina, L. Colucci-D'Amato, M. G. Reccia, F. Volpicelli, A. Parente, and A. Chambery, "Secretome profiling of differentiated neural mes-c-myc a1 cell line endowed with stem cell properties," *Biochimica et Biophysica Acta (BBA)-Proteins and Proteomics*, vol. 1834, no. 11, pp. 2385–2395, 2013.

[53] S. Shaphiro and M. Wilk, "An analysis of variance test for normality," *Biometrika*, vol. 52, no. 3, pp. 591–611, 1965.

[54] N. Shoham, P. Girshovitz, R. Katzengold, N. T. Shaked, D. Benayahu, and A. Gefen, "Adipocyte stiffness increases with accumulation of lipid droplets," *Biophysical Journal*, vol. 106, no. 6, pp. 1421–1431, 2014.

[55] S. Singh, L. L. Fujii, M. H. Murad, Z. Wang, S. K. Asrani, R. L. Ehman, P. S. Kamath, and J. A. Talwalkar, "Liver stiffness is associated with risk of decompensation, liver cancer, and death in patients with chronic liver diseases: a systematic review and meta-analysis," *Clinical Gastroenterology and Hepatology*, vol. 11, no. 12, pp. 1573–1584, 2013.

[56] G. S. Stein, J. B. Lian, A. J. Van Wijnen, J. L. Stein, M. Montecino, A. Javed, S. K. Zaidi, D. W. Young, J.-Y. Choi, and S. M. Pockwinse, "Runx2 control of organization, assembly and activity of the regulatory machinery for skeletal gene expression," *Oncogene*, vol. 23, no. 24, p. 4315, 2004.

[57] Y. Ujihara, M. Nakamura, H. Miyazaki, and S. Wada, "Segmentation and morphometric analysis of cells from fluorescence microscopy images of cytoskeletons," *Computational and mathematical methods in medicine*, vol. 2013, 2013.

[58] M. Unal, Y. Alapan, H. Jia, A. G. Varga, K. Angelino, M. Aslan, I. Sayin, C. Han, Y. Jiang, Z. Zhang *et al.*, "Micro and nano-scale technologies for cell mechanics," *Nanobiomedicine*, vol. 1, no. Godište 2014, pp. 1–5, 2014.

[59] J. K. Van Tam, K. Uto, M. Ebara, S. Pagliari, G. Forte, and T. Aoyagi, "Mesenchymal stem cell adhesion but not plasticity is affected by high substrate stiffness," *Science and technology of advanced materials*, vol. 13, no. 6, p. 064205, 2012.

[60] L. Vergani, "Lipid lowering effects of iodothyronines: in vivo and in vitro studies on rat liver," *World journal of hepatology*, vol. 6, no. 4, p. 169, 2014.

[61] N. Wang, J. D. Tytell, and D. E. Ingber, "Mechanotransduction at a distance: mechanically coupling the extracellular matrix with the nucleus," *Nature reviews Molecular cell biology*, vol. 10, no. 1, p. 75, 2009.

[62] X. Yang, S. Askarova, and J. C. Lee, "Membrane biophysics and mechanics in alzheimer's disease," *Molecular neurobiology*, vol. 41, no. 2-3, pp. 138–148, 2010.

[63] T. Zhang, Y. Zhao, Z. Tong, and Y. Guang, "A novel method to calculate the mechanical properties of cancer cells based on atomic force microscopy," *Acta of bioengineering and biomechanics*, vol. 18, no. 1, 2016.

[64] Y. Zhang, Y.-p. Zhao, and Z. Cheng, "Determining the layers' young's moduli and thickness from the indentation of a bilayer structure," *Journal of Physics D: Applied Physics*, vol. 51, no. 6, p. 065305, 2018.

[65] C. Zhu, G. Bao, and N. Wang, "Cell mechanics: mechanical response, cell adhesion, and molecular deformation," *Annual review of biomedical engineering*, vol. 2, no. 1, pp. 189–226, 2000.